LITHOS 460–461 (2023) 107391

Contents lists available at ScienceDirect

LITHOS

journal homepage: www.elsevier.com/locate/lithos

Unravelling the hydration history of an inverted passive continental margin using epidote U—Pb geochronology and Pb–Sr–O–H isotope geochemistry

Veronica Peverelli [a,*], Alfons Berger [a], Martin Wille [a], Andreas Mulch [b,c], Pierre Lanari [a], Thomas Pettke [a], Benita Putlitz [d], Marco Herwegh [a]

[a] Institute of Geological Sciences, University of Bern, Bern, Switzerland.
[b] Senckenberg Biodiversity and Climate Research Centre (SBiK-F), Frankfurt, Germany
[c] Goethe University Frankfurt, Institute of Geosciences, Frankfurt, Germany
[d] Institute of Earth Sciences, University of Lausanne, Lausanne, Switzerland

ARTICLE INFO

Keywords:
Epidote U—Pb geochronology
Epidote isotope geochemistry
Fluid circulation
Continental crust
Orogens

ABSTRACT

Inverted passive continental margins permit to comprehensively characterize fluid circulation in the continental crust in orogens from rifting to tectonic inversion. Since granitic rocks have low primary water contents and dominate the continental crust, their hydration exerts important control on metamorphism and deformation of the continental crust during orogeny. It is therefore of great interest to determine whether the granitic continental crust is hydrated during rifting phases or after tectonic inversion. Because fluid circulation may occur at both stages, a comprehensive picture of hydration of the continental crust in inverted passive continental margins can be obtained by the combination of different geochronometers and geochemical methods.

In this study, we combine U—Pb geochronology and Pb–Sr–O–H isotope geochemistry of epidote in hydrothermal veins in the Albula Pass area (eastern Swiss Alps) as powerful tools to trace hydration events in the continental crust in orogens. The Albula Pass area is part of the inverted Adriatic passive continental margin, which was extensively affected by seawater infiltration during continental rifting in Jurassic times. Epidote geochronology elucidates the fluid circulation history in this rifted crustal section by revealing two hydration events that are not recorded by other datable minerals: (1) 85.2 ± 9.7 Ma and (2) 59.9 ± 2.7 Ma, showing that fluid circulation in the Adriatic passive continental margin continued after Late Cretaceous tectonic inversion. Epidote Pb–Sr–O–H isotope geochemistry characterizes pathways and fluid sources of the epidote forming fluids, which differ between the Late Cretaceous and the Paleocene fluid circulation events. The Late Cretaceous epidote-forming fluids were produced by compaction of sedimentary units beneath the Err nappe and release of modified seawater (i.e., formation/connate water) from marine sediments, while Paleocene veining was mainly mediated by *syn*-kinematically infiltrated meteoric water. The present geochronological and isotope data argue for multi-stage hydration of the continental crust in the inverted Adriatic passive continental margin. This work promotes the importance of the interplay of newly introduced and recycled fluid components in the hydrothermal alteration of the continental crust, and it highlights epidote as a powerful hygrochronometer and isotope tracer.

1. Introduction

Granitoids dominate the continental crust and are mechanically strong in their pristine state. Their hydrothermal alteration induces prominent weakening, with important implications for the structural evolution of the continental crust during orogeny, particularly for strain localization (e.g., Airaghi et al., 2020; Bellahsen et al., 2019; Ferry, 1979; Manatschal et al., 2015; Morad et al., 2010; Oliot et al., 2010). Fluid circulation in, and fluid-driven alteration of, granitoids are therefore fundamental processes. A key knowledge gap is when water is introduced into these rocks so that hydrous minerals can be stabilized during metamorphism and deformation (e.g., Airaghi et al., 2020;

* Corresponding author at: Department of Biological, Geological and Environmental Sciences, Università degli Studi di Bologna, Bologna, Italy.
E-mail addresses: veronica.peverelli@unibe.ch (V. Peverelli), alfons.berger@unibe.ch (A. Berger), martin.wille@unibe.ch (M. Wille), andreas.mulch@senckenberg.de (A. Mulch), pierre.lanari@unibe.ch (P. Lanari), Thomas.pettke@unibe.ch (T. Pettke), benita.putlitz@unil.ch (B. Putlitz), marco.herwegh@unibe.ch (M. Herwegh).

https://doi.org/10.1016/j.lithos.2023.107391
Received 16 June 2023; Received in revised form 28 September 2023; Accepted 11 October 2023
Available online 14 October 2023

Bellahsen et al., 2019; Dusséaux et al., 2022; Goncalves et al., 2012; Grambling et al., 2022; Wehrens et al., 2016, 2017). Owing to low preservation potential, evidence for pre-orogenic fluid circulation is quite scant and limited to a few localities in the world (e.g., Airaghi et al., 2020; Incerpi et al., 2017, 2018, 2020; Manatschal et al., 2000, 2015; Peverelli et al., 2022a; Pinto et al., 2015). Attempts at compiling comprehensive sequences of fluid circulation in the granitic continental crust from rifting to orogeny are even scarcer (e.g., Peverelli et al., 2022a). However, such compilations would greatly improve our understanding of the water cycle in the granitic continental crust in orogens, which is – for example – a crucial aspect in the formation of ore deposits. In this respect inverted passive continental margins are excellent case studies because their evolution includes continental rifting, tectonic inversion and orogeny.

To reconstruct fluid circulation in crustal rocks, numerous studies use trace element, isotope and geochronological data of hydrothermal structures such as veins or hydrothermally deformed rocks (e.g., Dempster, 1986; Dusséaux et al., 2022; Grambling et al., 2022; Hofmann et al., 2004; Incerpi et al., 2017, 2018, 2020; Kralik et al., 1992; Manatschal et al., 2000; Marquer and Burkhard, 1992; Marquer and Peucat, 1994; Mulch et al., 2006; Peverelli et al., 2022a, 2022b; Pinto et al., 2015; Ricchi et al., 2019a, 2019b). One advantage of targeting vein-filling minerals for this purpose is that they precipitate directly from the mineralizing fluid, whose geochemical and isotopic characteristics are recorded and can be used to investigate fluid pathways (e.g., Bons et al., 2012; Elburg et al., 2002; Pettke et al., 2000). In the Alps, one common vein-filling mineral that is stable throughout the metamorphic evolution of the orogen at greenschist-facies conditions is epidote [i.e., $Ca_2Al_2(Al,Fe^{3+})Si_3O_{12}(OH)$]. This mineral is also produced during hydrothermal alteration of the crust during rifting of passive continental margins (e.g., Iberian Margin; Gardien and Paquette, 2004). The wide range of pressures (ca. 0.1–7 GPa), temperatures (ca. 250–1000 °C) and geodynamic settings across which epidote can be stable (Bird and Spieler, 2004; Enami et al., 2004; Franz and Liebscher, 2004; Grapes and Hoskin, 2004; Poli and Schmidt, 2004) make this mineral particularly useful to study fluid circulation in inverted passive continental margins. The high preservation potential of epidote to retain its crystallization age across deformation events was recently substantiated by the occurrence of variably deformed epidote veins in the central Swiss Alps (Peverelli et al., 2022a, 2022b). Strontium and Pb are readily incorporated by hydrothermal epidote from the mineralizing fluid, and substitute for Ca in the epidote crystal structure. Their isotopes can be used, in combination with those of O and H in the epidote hydroxyl group, to trace the geochemical characteristics of the epidote-forming fluids. This contribution presents in-situ U—Pb geochronology and Pb–Sr–O–H isotopic compositions of epidote in hydrothermal veins from the Err nappe (Eastern Swiss Alps). The Err nappe represents a classical example of hyperextended continental crust in a passive continental margin (Manatschal et al., 2015; Mohn et al., 2011, 2012). It is therefore an ideal target area to study when the continental crust was infiltrated by water during Jurassic rifting and (Eo-)Alpine inversion, possibly complementing the hydration history of an inverted passive continental margin. Notably, this work demonstrates the potential of epidote as a hygrochronometer (see Bosse and Villa, 2019) to date fluid circulation, and as an isotope tracer to investigate fluid pathways.

2. Geological context

The sampling location at the Albula Pass area is located on the boundary between the Err and Ela nappes (Figs. 1–2). Here, frequent epidote veins are hosted by the Albula Granite, a calc-alkaline granodiorite that represents the most common lithology in the Albula Pass area (e.g., Furrer et al., 2015; Manatschal and Nievergelt, 1997). The Albula Granite intruded the metamorphic basement of the Err nappe in late Carboniferous–early Permian times (Mohn et al., 2011). Besides Late- to Post-Variscan granitoids, the Err nappe includes middle Jurassic *syn*-rift siliciclastic sediments like the Saluver Breccia, which contains clasts of Albula Granite, limestones and dolomite (Froitzheim et al., 1994; Mohn et al., 2011). The Ela nappe is dominated by thick (120–1500 m; strati.ch) pre-rift (e.g., Triassic Mingér Formation and Hauptdolomit Group) and syn- to late-rift (e.g., Allgäu Formation) sediments (Mohn et al., 2011). The Mingér Formation belongs to the Raibl Group, which is constituted by dolomitic and evaporitic rocks deposited in Ladinian to Carnian times. The Hauptdolomit Group is of Carnian to Norian age, and it is dominated by massive and rarely brecciated dolomite. The Middle Jurassic Allgäu Formation consists of limestones and marls (Furrer et al., 2015). Mohn et al. (2011) relate this difference in sedimentary record to the position of these units during rifting, with the Err and Ela nappes representing, respectively, the distal and proximal margins. The rift evolution produced a hyper-extended continental margin and an ocean-continent transition by the Late Cretaceous, as recorded west of the study area (Froitzheim and Manatschal, 1996;

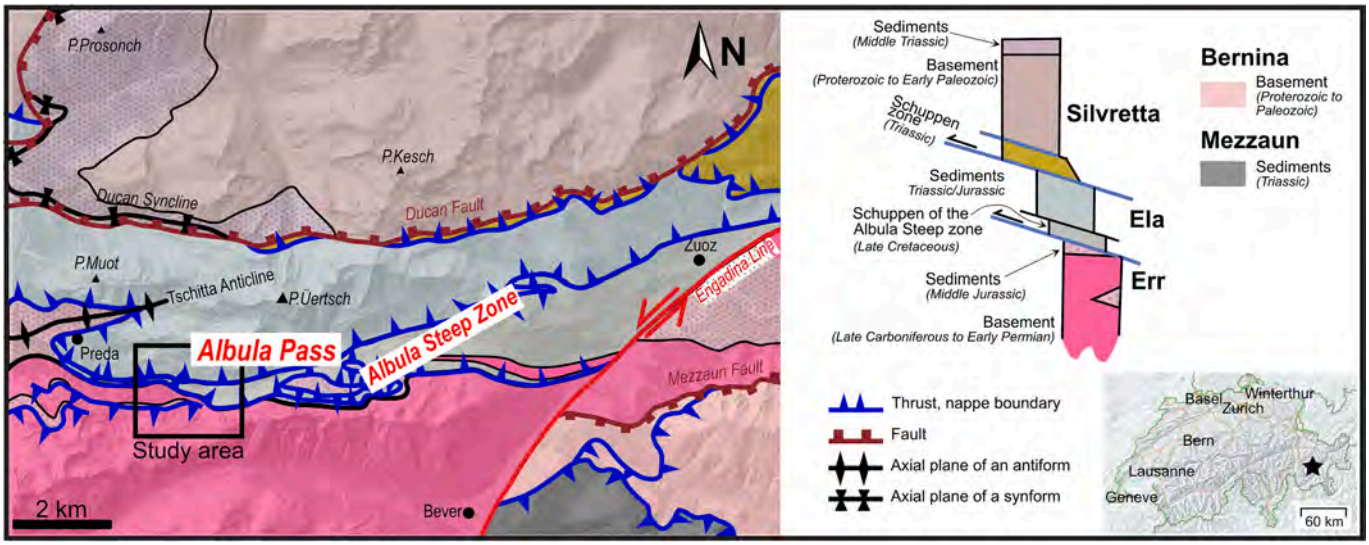

Fig. 1. Tectonic map of the Albula Pass area. The black rectangle shows the location of Fig. 2 (also black star in the geographic map of Switzerland). A tectonostratigraphic column (righthand side) shows the preserved geometry (thicknesses not to scale). Ages are from strati.ch (last access: 27 September 2023). Redrawn from Furrer et al. (2015); the digital elevation model is from map.geo.admin.ch (last access: 13 April 2023).

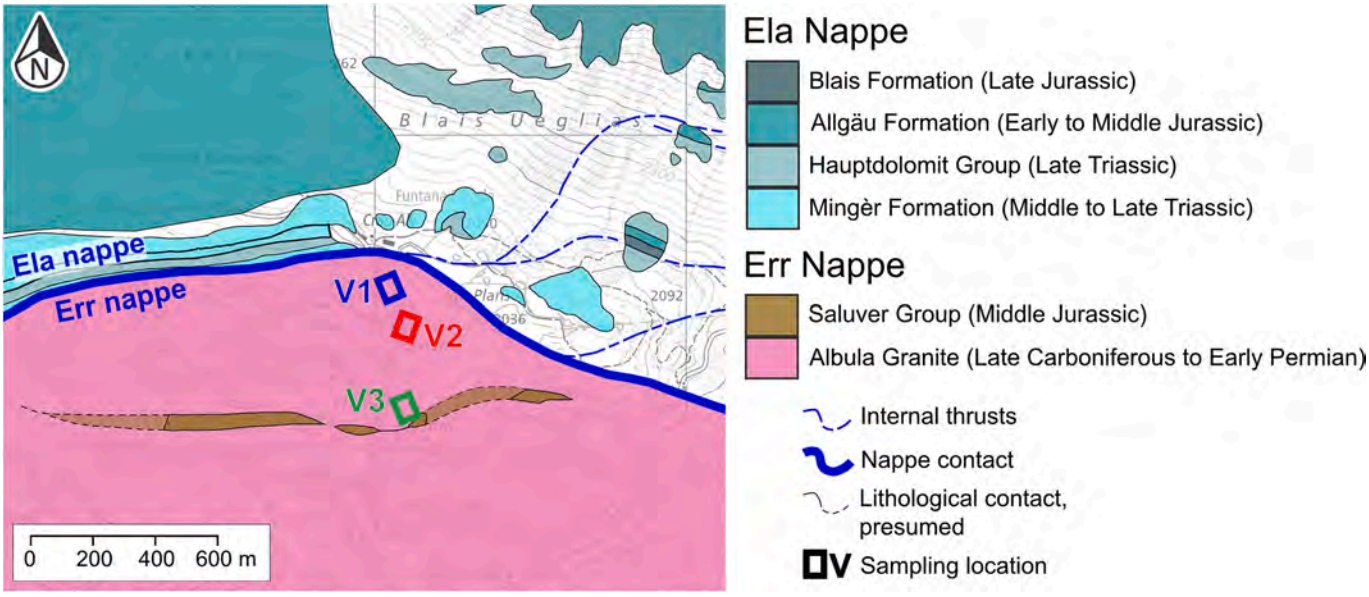

Fig. 2. Geological map of the sampling location. In addition to tectonic units (Fig. 1), the different lithologies of the Ela nappe are shown. Colorless areas are Quaternary sediments. Ages are from strati.ch (last access: 27 September 2023). Redrawn from map.geo.admin.ch (last access: 13 April 2023).

Manatschal and Nievergelt, 1997; Mohn et al., 2011). Lower Jurassic rifting is embodied by large-scale normal faults dissecting the basement, and by syn-rift breccias such as the Saluver breccia (Saluver Group in Fig. 2; Froitzheim et al., 1994; Manatschal and Nievergelt, 1997; Mohn et al., 2011). As demonstrated by Sr and O isotope data, this hyper-extended margin was hydrothermally altered during Jurassic rifting when seawater percolated into the crustal units down to ca. 10–14 km depth exploiting rift-related structures (e.g., Incerpi et al., 2017, 2018, 2020; Manatschal et al., 2000, 2015; Pinto et al., 2015).

Late Cretaceous tectonic inversion of the Adriatic passive continental margin is recorded in the study area by three main deformational phases (Table 1). Throughout orogeny, the area experienced lower greenschist-facies conditions, with only the Trupchun and Ducan–Ela phases occurring in the stability field of epidote at 300–350 °C and 250–300 °C, respectively (Handy et al., 1996). Pressures were previously estimated based on phengite geobarometry (i.e., Si in mica) at 800–900 MPa for Trupchun and at 400–500 MPa for Ducan–Ela at the base of the Err nappe (Handy et al., 1996). The Trupchun phase is related to the inversion of the passive continental margin with W- to NW-directed nappe stacking, during which the Ela nappe was thrust on top of the Err nappe (Froitzheim et al., 1994; Handy et al., 1996; Mohn et al., 2011). White mica K/Ar ages in the schistosity indicate that greenschist-facies metamorphism related to the Trupchun phase occurred ca. 80–88 Ma (Handy et al., 1996). The following Ducan–Ela phase took place ca. 80–67 Ma, as indicated by white mica K/Ar dating, and led to top-to-the-E normal faulting and extensional uplift (Froitzheim et al., 1994; Handy et al., 1996). This deformation phase is interpreted as resulting from extension in the hanging wall (Handy et al., 1996; Mohn et al., 2011). The Trupchun and Ducan–Ela structures accommodated deformation related to the Eo-Alpine orogeny. Finally, the Blaisun phase – here only mentioned cursorily because outside the stability field of epidote (< 250 °C; Handy et al., 1996) – was a response to the N–S-directed shortening upon continental collision between Adria and Europe in Eocene times (Handy et al., 1996; Mohn et al., 2011; and references therein). The weak Cenozoic tectono-metamorphic overprint in the Err nappe permitted the preservation of the earlier Eo-Alpine structures (e.g., Mohn et al., 2011). The Albula Pass area includes the "Albula steep zone" (Fig. 1), which is a late Trupchun structure: Here, the Ela nappe also lies tectonically below the Err nappe (Froitzheim et al., 1994). The formation of this zone and its role in accommodating deformation is debated, and it is beyond the scope of this work to propose alternative scenarios to that illustrated by Froitzheim et al. (1994).

Table 1
Main characteristics of the deformation phases that affected the study area between the Late Cretaceous and the Eocene. Phase and process are from Froitzheim et al. (1994), while ages, and temperature and pressure data are from Handy et al. (1996). Ep = epidote.

Phase[1]	Process	Age	Temperature[2]	Pressure[2]	Ep stability field
Trupchun (D1)	W-directed thrusting and folding	88–80 Ma[3]	300–350 °C	800–900 MPa	Yes
Ducan–Ela (D2)	E–W extension	80–67 Ma[3]	250–300 °C	400–500 MPa	Yes
Blaisun (D3)	N–S shortening	Eocene	150–250 °C	200–300 MPa	No

[1] In parentheses: nomenclature of Handy et al. (1996).
[2] At the base of the Err nappe (Handy et al., 1996).
[3] White mica K/Ar (Handy et al., 1996).

3. Samples

3.1. Epidote veins

The studied epidote vein samples were collected at localities shown in Fig. 2. The distinction of each epidote vein sample into V1, V2 and V3 vein groups is based on the appearance of the host rock in the field (Table 2): One V1 vein is hosted by coarse-grained and pale gray Albula Granite, and cuts through an enclosure of sandstone within the Albula Granite (Sect. 3.1; Fig. 3a). This sandstone pocket is ca. 1–4 cm wide and it is a local feature. V2 and V3 veins are hosted by the Albula Granite only, but with differing characteristics at the mesoscale: fine-grained and dark green granitoid (V2 samples; Fig. 3b), and coarse-grained and pale gray granitoid (V3 samples; Fig. 3c–d). The one V1 vein observed can reach a few mm in width, and has sharp, straight boundaries (Fig. 3a). V2 veins display sharp, planar boundaries and reach a maximum aperture of ca. 1 mm (Fig. 3b). V3 veins can reach a width of a few cm and cut the Albula Granite with different geometries: (1) sharp, straight boundaries (Fig. 3c), (2) convoluted with locally blurred

Table 2
Epidote veins studied here, with the subdivision into V1, V2 and V3 veins based on the appearance of their host rock.

Epidote vein sample	WGS84 coordinates	Orientation	Vein group	Host rock
ALB19–1	46°34′51″N 9°48′04″E	197/50	V1	Albula Granite + Sandstone enclosure
ALB19–4	46°34′45″N 9°48′04″E	020/89	V2	Cataclastic Albula Granite
Albula-1	46°34′36″N 9°48′05″E	Not meas. (steep)	V3	Weakly foliated and deformed Albula Granite
ALB19–11		180/ 75–130/85[1]		
ALB19-18		170/65		

[1] Orientation is variable because the vein is not planar.

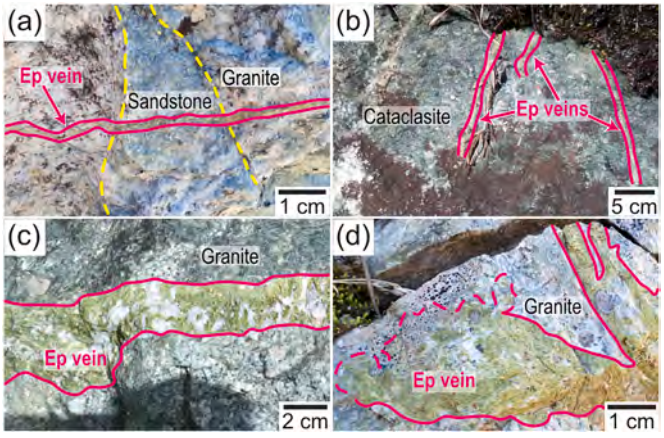

Fig. 3. Field view of the epidote vein samples. (a) V1 vein ALB19–1 crosscutting a sandstone enclosure in the Albula Granite ("Granite"). (b) V2 veins ALB19–4 in cataclastic Albula Granite ("Cataclasite"). V3 veins (c) Albula-1 and (d) ALB19–11 in weakly foliated Albula Granite ("Granite"). Ep = epidote.

boundaries (Fig. 3d), or (3) a combination of both (Figs. 3c). For the present study, one V1 epidote vein (one studied sample), two V2 epidote veins (in one studied hand sample), and four V3 epidote veins (in three studied hand samples) were selected. No meso- or microstructural characteristics of the veins allow us to infer the relative or absolute timing of vein formation.

3.1.1. V1 epidote vein

The selected V1 epidote vein (sample ALB19–1; Fig. 4a) is composed of epidote and quartz. In thin section, the host rock is a sandstone composed of rounded quartz and saussuritic/sericitized feldspars (i.e., plagioclase and alkali feldspar) of roughly the same dimensions (diameters of ca. 200–800 μm for quartz and ca. 200–300 μm for feldspars). Vein growth microstructures from blocky to elongate are preserved (Fig. 5; nomenclature after Bons et al., 2012). Epidote is euhedral to subhedral, and measures between a few and ca. 800 μm. Vein quartz ranges between ca. 0.2–2 mm and has undulose extinction. Sharp boundaries separate epidote and quartz grains. In backscattered electron (BSE) images (Fig. 8a), epidote grains display complex and sector chemical zoning, and rare cracks.

3.1.2. V2 epidote vein group

The Albula Granite with a cataclastic texture is the host of V2 epidote veins (sample ALB19–4; Fig. 4b). The host rock is composed of quartz, feldspars and white mica, whose relative proportions are difficult to estimate due to feldspar alteration. Outside the cataclastic portions of the host granitoid, quartz (0.2–1.2 mm) is anhedral and has undulose extinction. Feldspar grains (80 μm to 3.5 mm) are anhedral and slightly altered. White mica dominates the fine-grained aggregates of feldspars

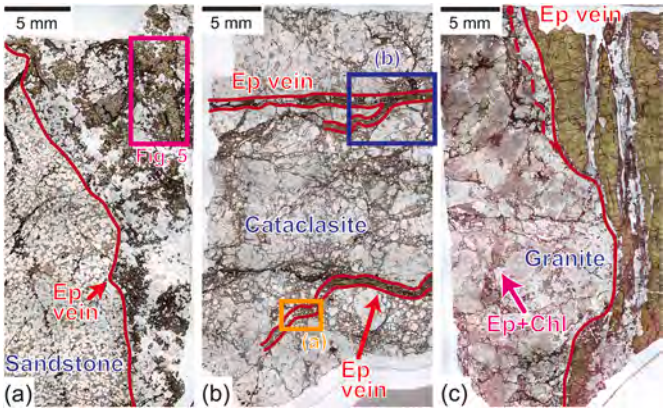

Fig. 4. Transmitted-light microphotographs of (a) V1 vein ALB19–1 in sandstone, (b) V2 veins ALB19–4 in cataclastic Albula Granite, and (c) V3 vein ALB19–11 in weakly deformed Albula Granite with a weak foliation of epidote + chlorite (pink arrow). Rectangles in a–b in panel (b) indicate the locations of the microphotographs of Figs. 5–3. The dashed red curve in panel (c) indicates a level of plagioclase. Chl = chlorite; Ep = epidote. Plane-polarized light. (For interpretation of the references to colour in this figure legend, the reader is referred to the web version of this article.)

and quartz defining the cataclasites, and wraps feldspar relicts; a few grains (80–800 μm) with undulose extinction are disseminated in the rock. V2 veins have similar orientation (Table 2), as well as morphological and mineralogical characteristics. The morphology of V2 epidote veins varies from blocky to elongate (Fig. 6). These veins are constituted of euhedral to subhedral epidote grains of a few to ca. 500 μm, and quartz. Quartz measures ca. 100–200 μm and has slight undulose extinction. Epidote-quartz grain boundaries are sharp (Figs. 3b, 4b and 6). Cataclastic portions are crosscut by V2 veins (Fig. 6b, red arrow), indicating that veining occurred after cataclasis. Moreover, epidote veins locally grow exploiting discontinuities produced by cataclasis (Fig. 6b, dashed curves). The veins preserve their growth microstructures, as also indicated by sector chemical zoning in BSE images (Fig. 8b), despite a few cracks in epidote.

3.1.3. V3 epidote vein group

V3 epidote veins are hosted by weakly foliated and deformed Albula Granite (Figs. 3c and 4c). Magmatic feldspars (ca. 0.2–3 mm) are highly altered into sericite and saussurite, with rare plagioclase relicts recognizable. A weak foliation defined by chlorite + epidote ± plagioclase (Fig. 4c, pink arrow) indicates metamorphism at greenschist-facies conditions, which are also attested to by the mineral assemblages of V3 veins (see below). Quartz (ca. 0.2–1 mm) displays undulose

Fig. 5. Transmitted-light microphotograph of V1 vein ALB19–1. Ep = epidote; Qz = quartz. Red curve = vein–host boundary. Plane-polarized light. (For interpretation of the references to colour in this figure legend, the reader is referred to the web version of this article.)

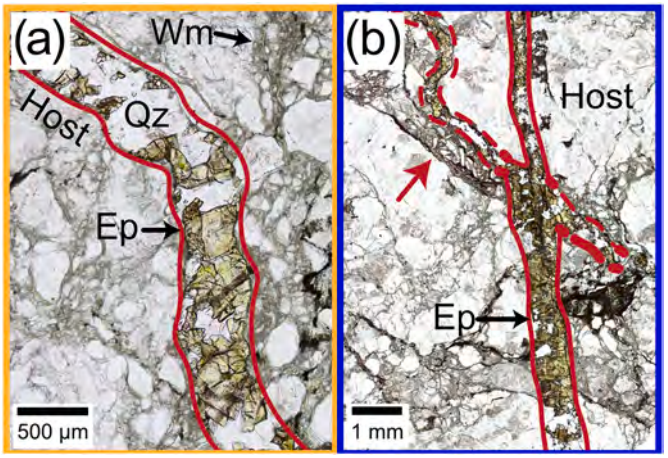

Fig. 6. Transmitted-light microphotographs of V2 veins in sample ALB19–4 cutting a cataclasite (red arrow in panel b). Dashed red curves = ill-defined vein-host boundaries. Ep = epidote; Wm = white mica. Plane-polarized light. (For interpretation of the references to colour in this figure legend, the reader is referred to the web version of this article.)

extinction in all samples. Locally, the vein–host boundary is marked by a band of plagioclase with twinning perpendicular to the direction of vein opening (Fig. 4c, dashed red line). Three types of V3 veins are recognized (Fig. 7).

The first type is represented by sample Albula-1 (Fig. 7a–b; "Vein1" presented by Peverelli et al., 2021). This vein has epidote grains with lengths between ca. 0.5 mm close to the vein boundaries and ca. 1 cm in the center of the vein, with aspect ratios up to 7:1. The vein morphology varies from blocky at the vein rims to elongate towards the center (Fig. 7b). The smaller epidote crystals define a band along the vein boundaries where epidote is associated with plagioclase (ca. 400–800 μm) with twinning perpendicular to the vein boundary (black arrow in Fig. 7a). Outside this band, epidote is associated with fractured quartz measuring ca. 1.2–6 mm. Epidote grains are mostly euhedral, attesting to the preservation of growth microstructures, which is also confirmed by sector chemical zoning in BSE images (Fig. 8c). Only Vein1 (Fig. 7a) is addressed and used for the isotope analyses presented in this contribution. However, a secondary vein (Vein2; Fig. 7a) is recognized in sample Albula-1, with a width of ca. 1 mm in which euhedral to subhedral epidote grains (ca. 1–2 mm) are associated with quartz and plagioclase. Peverelli et al. (2021) obtained an LA-ICP-MS U—Pb age of 62.7 ± 3.0 Ma with an initial $^{207}Pb/^{206}Pb$ ratio of 0.8334 ± 0.0043 from datapoints in epidote in both veins, which singularly gave ages and initial $^{207}Pb/^{206}Pb$ ratios that are indistinguishable within uncertainty.

The second type of V3 veins – sample ALB19–11 (Fig. 7c–d) – is constituted of euhedral/subhedral epidote grains with minor and interstitial chlorite (ca. 150 μm to 1.5 mm), quartz (ca. 400–600 μm) and plagioclase (ca. 80–600 μm). Local fracturing causes ill-defined vein boundaries, which are otherwise sharp and sinuous (Fig. 7c). The blocky microstructure makes it difficult to estimate the maximum size of single epidote grains, exceeding 500 μm (Figs. 7d and 8c), whereas the minimum size is ca. 100 μm. The preservation of growth microstructures is supported by perfectly euhedral smaller epidote grains and by intact sector and complex chemical zoning in BSE images of epidote grains (Fig. 8c).

Finally, V3 sample ALB19–18 (Fig. 7e–g) can be subdivided into two domains: (a) an epidote + quartz + plagioclase vein (Fig. 7e) and (b) 1–5 mm wide pockets filled by epidote + chlorite + quartz ± plagioclase (Fig. 7g) disseminated throughout the country rock. In the host rock, magmatic feldspars are completely altered, preventing their full description, but sericitized/saussuritic feldspar pseudomorphs reaching up to 6 mm in diameter are recognized (Fig. 7f–g). Domain (a) of the epidote vein shows epidote bands alternating with quartz + plagioclase

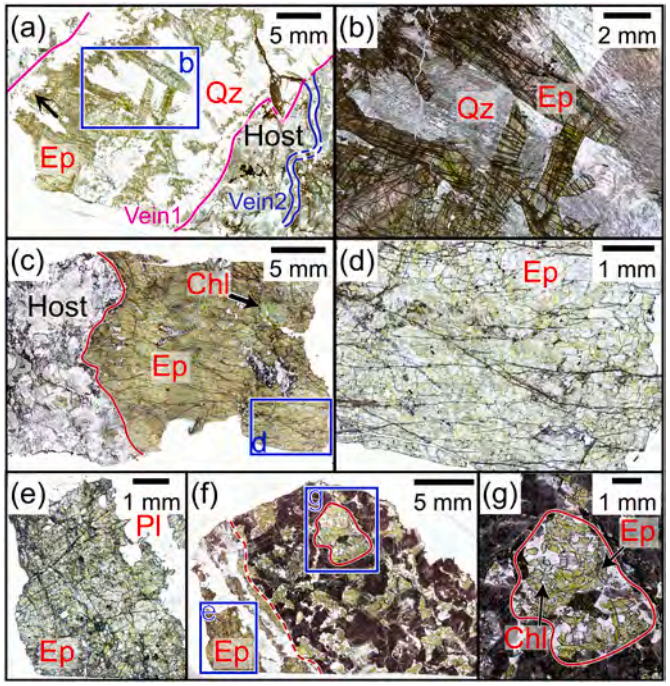

Fig. 7. Transmitted-light microphotographs of V3 veins (a–b) Albula-1, (c–d) ALB19–11, and (e–f) ALB19–18. The black arrow in panel (a) indicates a level of plagioclase. Chl = chlorite; Ep = epidote; Pl = plagioclase; Qz = quartz. Blue rectangles indicate panels in the present figure. Plane-polarized light. (For interpretation of the references to colour in this figure legend, the reader is referred to the web version of this article.)

± minor chlorite in a blocky vein morphology (Fig. 7e). Epidote grains have minimum sizes of ca. 20 μm, while the largest grains exceed 400 μm. Quartz (ca. 0.4–4 mm) has undulose extinction, and the twinning of plagioclase (ca. 0.4–1.5 mm) is perpendicular to the vein–host boundary. The vein morphology of domain (b) cannot be referred to any classical microstructures (Fig. 7g; see Bons et al., 2012). Epidote in domain (b) is euhedral with lengths between ca. 200 μm and ca. 1 mm. In this domain, plagioclase, chlorite, and quartz measure ca. 80 μm to 1.2 mm, 40–200 μm and 0.8–1 mm, respectively. Growth microstructures are preserved in both domains despite some fracturing, as supported by intact sector and complex chemical zoning (Fig. 8e–f).

3.2. Bedrock samples

To assess the pathways of the epidote-forming fluids using Sr and Pb isotopes, samples of gneissic Albula Granite and carbonate rocks of the Ela nappe (i.e., Allgäu and Mingér Formations, and Hauptdolomit Group; hereafter, collectively referred to as "carbonate rocks") were collected in the surroundings of the V1–V3 sampling locations. The Albula Granite sample is collected from the sampling location of V3 epidote veins: it does not contain epidote veins, but it is intensely saussuritized (see Sect. 4.3). The samples of the Allgäu and Mingér Formations are dark gray with rare calcite veins (i.e., < 5–10 in ca. 500 cm^3 hand samples), which are common in the light gray Hauptdolomit sample (i.e., 10–20 in a ca. 300 cm^3 hand sample).

4. Methods

Analyses were carried out at the Institute of Geological Sciences, University of Bern, unless specified. The petrographic characterization of the samples was made on a ZEISS Axioplan microscope and on a Zeiss EVO50 scanning electron microscope (ca. 1 nA beam current, 20 kV acceleration voltage, and working distances of 8.5–9.5 mm). Details of

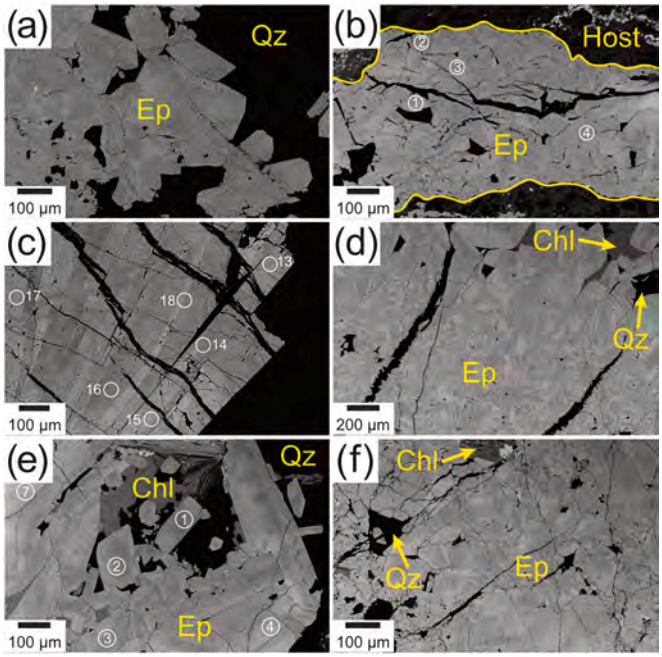

Fig. 8. Backscattered electron (BSE) images of epidote in (b) V1 vein ALB19–1, (b) V2 vein ALB19–4, and V3 veins (c) Albula-1, (d) ALB19–11), (e) domain (b) of ALB19–18 and domain (a) of ALB19–18. Chl = chlorite; Ep = epidote; Qz = quartz. The numbered yellow circles indicate 50 µm laser spots for U—Pb dating by LA-ICP-MS (Table B2). (For interpretation of the references to colour in this figure legend, the reader is referred to the web version of this article.)

analytical methods are in Appendix A.

4.1. Epidote U—Pb geochronology by LA-ICP-MS

The protocol outlined in Peverelli et al. (2021) was employed for U—Pb dating of the studied epidote samples by laser ablation inductively coupled plasma mass spectrometry (LA-ICP-MS). Analytical conditions are reported in Table A1 (Appendix A.1). Tara allanite (Gregory et al., 2007; Smye et al., 2014) was used as primary reference material. CAP (Barth et al., 1994; Gregory et al., 2007), CAP^b (Burn et al., 2017) and AVC (Barth et al., 2004; Gregory et al., 2007) allanite samples were analyzed as unknowns for quality control, obtaining U—Pb ages within uncertainty of, or sufficiently close to, their reference values (see Fig. B1 and Table A2; data in Table B3). Long-term reproducibility of CAP and CAP^b allanite is 1.9%, while that of AVC allanite 2.2%, and they are not propagated onto age uncertainties of the epidote unknowns as propagation produces negligible differences (see Appendix A.1). Data reduction was carried out in Iolite (version 7.08) and age calculation in Isoplot 3.7.5 (Ludwig, 2012).

4.2. Epidote Sr data by TIMS

Measurements of Sr isotopes were performed by thermal ionization mass spectrometry (TIMS) in epidote microseparates produced from each epidote vein. Before collecting the Sr fraction by ion chromatography using a Sr-spec™ resin (Horwitz et al., 1992), the samples were digested in acids following the procedure in Peverelli et al. (2021) modified from Nägler and Kamber (1996). The SRM987 standard was used for quality control, and for corrections for within-run mass bias and interference of ^{87}Rb during measurements by TIMS.

4.3. Strontium and Pb isotopes in Albula Granite and carbonate rocks

Hand samples of Albula Granite and carbonate rocks were dissolved in acids, but the silicate fraction of the carbonate samples was not dissolved. The Sr and Pb fractions were collected in sequence by ion chromatography. Strontium isotopes of the Albula Granite were measured by TIMS, with the analytical protocol used for epidote samples. Lead isotope ratios of granitoid and carbonate rocks, and Sr isotope data of the carbonate samples were measured by solution MC-ICP-MS. For Pb isotope measurements, a Tl spike was used to correct for instrumental mass fractionation. The SRM981 standard was used to assess external reproducibility of Pb isotope measurements. For quality control of Sr isotope data and for mass-bias correction, the SRM987 standard (Weis et al., 2006) was measured at the beginning and at the end of measurement sequences.

Granitoids and carbonate rocks can contain appreciable mass fractions of U and Rb, which decay into Pb and Sr, respectively, modifying the initial Pb and Sr isotope composition of the rock. Measurements of U/Pb and Rb/Sr ratios permit to apply the equations for radioactive decay of ^{235,238}U and ^{87}Rb into, respectively, ^{207,206}Pb and ^{87}Sr, and to calculate the ^{207}Pb/^{206}Pb and ^{87}Sr/^{86}Sr ratios at the desired time – the time of epidote vein formation in the present study. For this purpose, an aliquot of the dissolved samples of Albula Granite and carbonate rocks was collected before ion chromatography for measurements of Rb, Sr, U and Pb concentrations on a 7700× Agilent quadrupole ICP-MS at the Department of Geography of University of Bern.

4.4. Stable isotope data of epidote and estimates of crystallization temperature

Measurements of hydrogen isotopic ratios were performed using ca. 4 mg of epidote material at the Joint Goethe University Frankfurt–Senckenberg BiK-F Stable Isotope Facility (Frankfurt, Germany) on a Thermo high-temperature conversion elemental analyzer (TC/EA) coupled to a Thermo MAT 253 mass spectrometer in continuous flow mode. Repeated measurements of standards and unknowns resulted in an uncertainty of ±3 ‰ in δD values. Oxygen isotope ratios were measured at University of Lausanne (Switzerland) on single epidote grains handpicked from crushed vein material, using a CO_2-laser based extraction line coupled to a Finnigan MAT 253. Replicate measurements of unknowns indicate a precision of ±0.3 ‰ or better. Oxygen and H isotope ratios are expressed in ‰ relative to the Vienna Standard Mean Oceanwater (V-SMOW).

For calculation of δD and δ^{18}O values of epidote-forming fluids from the isotope data measured in epidote grains, estimated temperatures of epidote crystallization are necessary. For V3 epidote, the chemical composition of chlorite in textural equilibrium with epidote in sample ALB19–11, measured by electron probe microanalyzer (specimen current of 20 nA), was used to calculate the temperature of crystallization using the method of Vidal et al. (2005, 2006) implemented in the program ChlMicaEqui (Lanari, 2012). For V1 and V2 epidote, temperature estimates are outlined in Sect. 5.3. Hydrogen and oxygen isotope compositions of epidote-forming fluids are calculated following Chacko et al. (1999) and Zheng (1993), respectively.

5. Results

Table 3 summarizes U—Pb ages and Pb—Sr isotopic ratios of all epidote samples. In Table 3, Pb—Sr isotope ratios of host Albula Granite and of the carbonate rocks are presented as values at the time of epidote-forming fluid–rock interaction (see Table B1 in Appendix B for the measured uncorrected data). All epidote U—Pb age uncertainties are given at 95% confidence level, and all uncertainties in isotope ratios are 2 standard errors (2 S.E.) unless specified.

5.1. Epidote U—Pb geochronology

The ^{238}U/^{206}Pb and ^{207}Pb/^{206}Pb ratios obtained by LA-ICP-MS are presented in Tables B2 (Appendix B). In addition to a U—Pb age, the Tera–Wasserburg plot gives the ^{207}Pb/^{206}Pb ratio of initial Pb (i.e., Pb

Table 3
Tera–Wasserburg intercept ages, with MSWD and number of analyses (n), and Pb and Sr isotope ratios of epidote rock samples at the time of veining. All uncertainties are 2 standard errors (2 S.E.). To obtain the propagated 2 S.E. of average values, the 2 S.E. of individual ratios are propagated in quadrature. in = at the time of epidote vein formation.

	Sample	$^{238}U/^{206}Pb$ intercept age[1]	MSWD and number of analyses (n)	$(^{207}Pb/^{206}Pb)_{in}$	$(^{87}Sr/^{86}Sr)_{in}$
V1 Ep	ALB19–1	(22 ± 64 Ma)	MSWD = 1.01; n = 24	0.8201 ± 0.0018	0.713812 ± 0.000006
V2 Ep	ALB19–4	85.2 ± 9.7 Ma	MSWD = 0.78; n = 23	0.8083 ± 0.0017	0.714963 ± 0.000011
V3 Ep	ALB19–11	57 ± 18 Ma	MSWD = 1.4; n = 37	0.8289 ± 0.0019	0.713060 ± 0.000006
	ALB19–18 (a)	57 ± 11 Ma	MSWD = 0.89; n = 32	0.8232 ± 0.0014	0.713235 ± 0.000007
	ALB19–18 (b)				0.712983 ± 0.000004
	Albula-1[2]	62.7 ± 3.0 Ma	MSWD = 1.6; n = 22	0.8334 ± 0.0043	0.713835 ± 0.000005
Host	Albula Granite	Permian[2]	–	0.821157 ± 0.000025 (propagated 2 SE)	0.717611 ± 0.000011 (propagated 2 SE)
Carb.	Allgäu Fm.	Jurassic[3]	–	0.836553 ± 0.000028 (propagated 2 SE)	0.707448 ± 0.000014
rocks	Mingér Fm.	Triassic[3]	–	0.821744 ± 0.000019 (propagated 2 SE)	0.707745 ± 0.000012
	Hauptdolomit	Triassic[3]	–	0.836220 ± 0.000030 (propagated 2 SE)	0.712967 ± 0.000013

[1] Uncertainties do not include long-term reproducibility of secondary reference materials (between 1.9 and 2.2%). Please refer to the Supplementary material for details.
[2] "Vein1" of Peverelli et al. (2021).
[3] See Mohn et al. (2011) and strati.ch.

assimilated by epidote during crystallization), which can be used to assess the nature of the epidote-forming fluids (Sect. 6.2).

V1 epidote (sample ALB19–1) gave a lower intercept of 22 ± 64 Ma (MSWD = 1.10; number of analyses, n = 24) in a Tera–Wasserburg diagram (Fig. 9a). The uncertainty on this value (± 290%) is too large for the lower intercept to yield a meaningful age. This is due to the single analyses being dominated by initial Pb and containing negligible radiogenic Pb (i.e., high f206; Table B2). The initial $^{207}Pb/^{206}Pb$ ratio obtained from the Tera–Wasserburg plot is 0.8201 ± 0.0018.

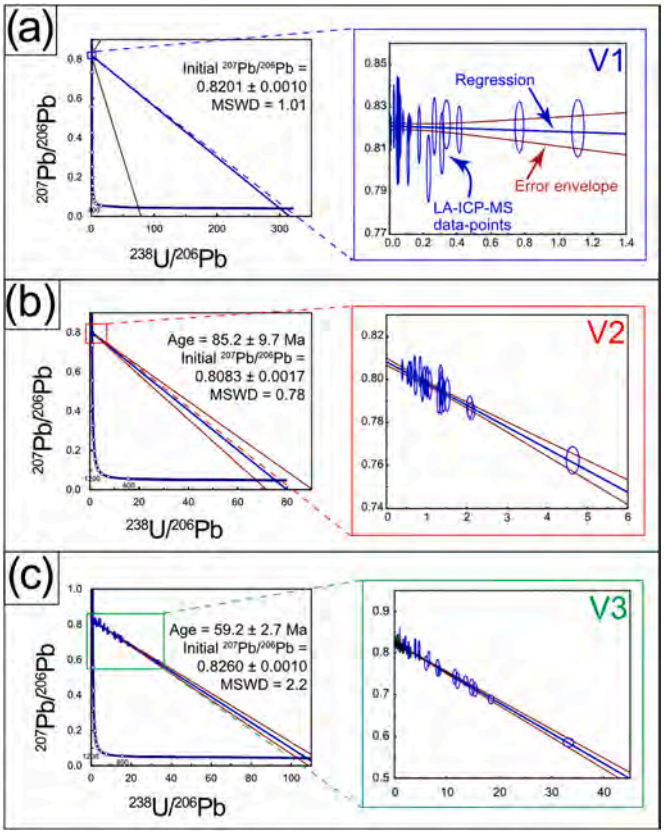

Fig. 9. Tera–Wasserburg diagrams of (a) V1 epidote in one epidote vein (ALB19–1), (b) V2 epidote in two epidote veins (ALB19–4), and (c) V3 epidote in three epidote veins (Albula-1, ALB19–11 and ALB19–18(a–b). Age uncertainties are at 95% confidence level and error ellipses are 2σ. Plotted with Isoplot 3.7.5 (Ludwig, 2012).

V2 epidote (sample ALB19–4) returned a Tera–Wasserburg date of 85.2 ± 9.7 Ma (MSWD = 0.78; n = 23), and an initial $^{207}Pb/^{206}Pb$ ratio of 0.8083 ± 0.0017 (Fig. 9b).

As for V3 epidote veins, ALB19–11 epidote yielded a Tera–Wasserburg date of 57 ± 18 Ma (MSWD = 1.4; n = 37) with an initial $^{207}Pb/^{206}Pb$ ratio of 0.8289 ± 0.0019 (Fig. B2a), and ALB19–18 epidote an age of 57 ± 11 Ma (MSWD = 0.89; n = 32) with an initial $^{207}Pb/^{206}Pb$ ratio of 0.8232 ± 0.0014 (Fig. B2b). No difference can be resolved either in date or in initial $^{207}Pb/^{206}Pb$ ratio in sample ALB19–18 by plotting the data obtained from microstructural domains (a) and (b) (Sect. 3.1.3). The Tera–Wasserburg date and initial $^{207}Pb/^{206}Pb$ ratio of sample Albula-1 of, respectively, 62.7 ± 3.0 Ma and 0.8334 ± 0.0043 are taken from Peverelli et al. (2021). If the datasets obtained from all V3 epidote samples (i.e., ALB19–11, ALB19–18 and Albula-1) are combined in a single Tera–Wasserburg plot, a date of 59.9 ± 2.7 Ma and an initial $^{207}Pb/^{206}Pb$ ratio of 0.8260 ± 0.0010 are obtained with an MSWD of 2.2 (n = 91; Fig. 9c). Although these three samples should be considered separately due to their different initial $^{207}Pb/^{206}Pb$ ratios, the fact that the MSWD value of the combined dataset remains sufficiently low permits to infer that these three vein samples formed during a fluid circulation stage at ca. 60 Ma at greenschist-facies conditions. Both lower intercepts and initial $^{207}Pb/^{206}Pb$ ratios of the Tera–Wasserburg regression of the three V3 epidote samples are outside the uncertainties of the same values obtained from the Tera–Wasserburg regression of V2 epidote. This suggests two clearly distinct veining events in the continental crust of the Err nappe between the Late Cretaceous and the Paleocene.

The presence of regular chemical zoning (Fig. 8) and the preservation of growth microstructures (Figs. 5–8) provide evidence that these dates are not the result of partial resetting of the U—Pb system during – for example – fluid-driven recrystallization of epidote. It has been shown that the U—Pb system is not reset in epidote relicts affected by (partial) recrystallization or dissolution–precipitation processes (Peverelli et al., 2022a, 2022b). Moreover, thermal diffusion of Pb and other trace elements would require much higher temperatures than those recorded by the study area during its geological history (< 350 °C; see Dahl, 1997; Franz and Liebscher, 2004). Additionally, no microstructural evidence suggests that the epidote veins may have been disturbed by secondary fluids after crystallization. Therefore, these dates are considered as ages of epidote crystallization during veining, and they will be discussed as veining ages in Sect. 6.1.

5.2. Strontium and Pb isotope data

The initial $^{207}Pb/^{206}Pb$ ratios of epidote are obtained from

Tera–Wasserburg diagrams (Sect. 5.1). The Sr isotope ratios of epidote by TIMS (Table 3) do not require age corrections because Rb is highly incompatible in epidote (see Feineman et al., 2007; Frei et al., 2004). Because ingrown ^{87}Rb-derived ^{87}Sr is negligible, the measured and the initial $^{87}Sr/^{86}Sr$ are equal. Epidote samples returned initial $^{207}Pb/^{206}Pb$ ratios between 0.0.8083 ± 0.0017 and 0.8334 ± 0.0049, and (initial) $^{87}Sr/^{86}Sr$ ratios between 0.712983 ± 0.000004 and 0.714963 ± 0.000011. These isotope ratios reflect the Pb—Sr isotope composition of the epidote-forming fluids and are used to evaluate fluid pathways.

The U and Rb contents (with $^{238}U/^{204}Pb$ of 21.8 and $^{87}Rb/^{87}Sr$ of 0.40) of the Albula Granite imply that its Pb and Sr isotope compositions differ significantly between the values measured today (0.811302 ± 0.000018 and 0.718021 ± 0.000007, respectively) and those calculated at the time of V2 epidote formation (t_{V2} = 85 Ma; $(^{207}Pb/^{207}Pb)_{tV2}$ = 0.822884 ± 0.000018; $(^{87}Sr/^{86}Sr)_{tV2}$ = 0.717541 ± 0.000007) and V3 epidote formation (t_{V3} = ca. 60 Ma; $(^{207}Pb/^{207}Pb)_{tV3}$ = 0.819430 ± 0.000018; $(^{87}Sr/^{86}Sr)_{tV3}$ = 0.717682 ± 0.000007). The $^{207}Pb/^{206}Pb$ and $^{87}Sr/^{86}Sr$ ratios of the Albula Granite presented in Table 3 of, respectively, 0.821157 ± 0.000025 and 0.717611 ± 0.000011 are average values of the ratios calculated at 60 Ma and 85 Ma. The uncertainties in the average values are calculated in quadrature from the uncertainties (as 2 S.E.) in the individual isotope ratios at t_{V1} and t_{V3}. The $^{87}Sr/^{86}Sr$ value (0.718021 ± 0.000007), with Rb and Sr mass fractions (11 and 78 μg g^{-1}, respectively; Table B1) measured in the Albula Granite sample returned an initial $^{87}Sr/^{86}Sr$ value (300 Ma) of 0.716324 ± 0.000007. This value is within the range of initial $^{87}Sr/^{86}Sr$ ratios obtained from the data of Pinto (2014) and Pinto et al. (2015). No Pb isotope data are available in the literature for the Albula Granite for comparison.

Similar considerations are valid for the Pb isotope composition of the carbonate rocks of the Ela nappe, whose $^{238}U/^{204}Pb$ ratios are 0.6–6.8. Hence, the $^{207}Pb/^{206}Pb$ ratios of the selected samples (Table 3) are average values calculated at 60 Ma (Allgäu Fm. = 0.835967 ± 0.000020; Mingér Fm. = 0.821206 ± 0.000013; Hauptdolomit = 0.836171 ± 0.000021) and 85 Ma (Allgäu Fm. = 0.837139 ± 0.000020; Mingér Fm. = 0.822283 ± 0.000013; Hauptdolomit = 0.836269 ± 0.000021) as outlined above. The low $^{87}Rb/^{87}Sr$ ratios (0.002–0.018) entail that the differences in $^{87}Sr/^{86}Sr$ ratios among the measured value, and those calculated at 60 Ma (Allgäu Fm. = 0.707447 ± 0.000014; Mingér Fm. = 0.707738 ± 0.000012; Hauptdolomit = 0.712951 ± 0.000013) and 85 Ma (Allgäu Fm. = 0.707446 ± 0.000014; Mingér Fm. = 0.707735 ± 0.000012; Hauptdolomit = 0.712945 ± 0.000012) are within the uncertainty of the measurements (Allgäu Fm. = 0.707448 ± 0.000014; Mingér Fm. = 0.707745 ± 0.000012; Hauptdolomit = 0.712967 ± 0.000013). Therefore, the $^{87}Sr/^{86}Sr$ data of the carbonate rocks (Table 3) are presented uncorrected.

The samples of Allgäu and Mingér limestones returned (initial) $^{87}Sr/^{86}Sr$ ratios that are consistent with formation in equilibrium with seawater in Triassic to Jurassic times ($^{87}Sr/^{86}Sr$ ratios of 0.7068–0.7080; McArthur et al., 2012). Conversely, the Hauptdolomit sample gave an initial $^{87}Sr/^{86}Sr$ value that is more radiogenic (i.e., higher) than Triassic seawater and published data (e.g., Faure et al., 1978). This is attributed to the presence of calcite veins in the hand samples (see Sect. 3.2). Since the time of formation of these calcite veins is unknown, particularly relative to veining, the Hauptdolomit sample with the obtained Pb—Sr isotope data is a plausible source of (partial) isotope equilibration for the epidote-forming fluids. No Pb isotope data are reported in the literature for the analyzed carbonate rocks.

In a $^{207}Pb/^{206}Pb$ vs. $^{87}Sr/^{86}Sr$ diagram (Fig. 10) plotting isotope ratios of epidote and bedrock samples at the time of epidote vein formation (i.e., 85–60 Ma), the Pb—Sr isotope data of V1 and V3 epidote veins are within the range defined by Albula Granite and carbonate rocks. Although the $^{87}Sr/^{86}Sr$ ratio of V2 epidote also is, its initial $^{207}Pb/^{206}Pb$ ratio is far more radiogenic.

5.3. $\delta^{18}O$ and δD data of V1–V3 of epidote samples and epidote-forming fluids

The $\delta^{18}O$ and δD values of the epidote samples range from 7.6 to 12.7 (± 0.3) ‰, and − 59 to −47 (± 3) ‰, respectively (Table 4). The stable isotope composition of domain (b) of V3 epidote vein ALB19–18 (see Sect. 3.3) was not measured because pure epidote separates, which are required for measurements, could not be produced for this microstructural domain. The measured values are used to calculate the $\delta^{18}O$ and δD data of epidote-forming fluids (Table 4) following Zheng (1993) and

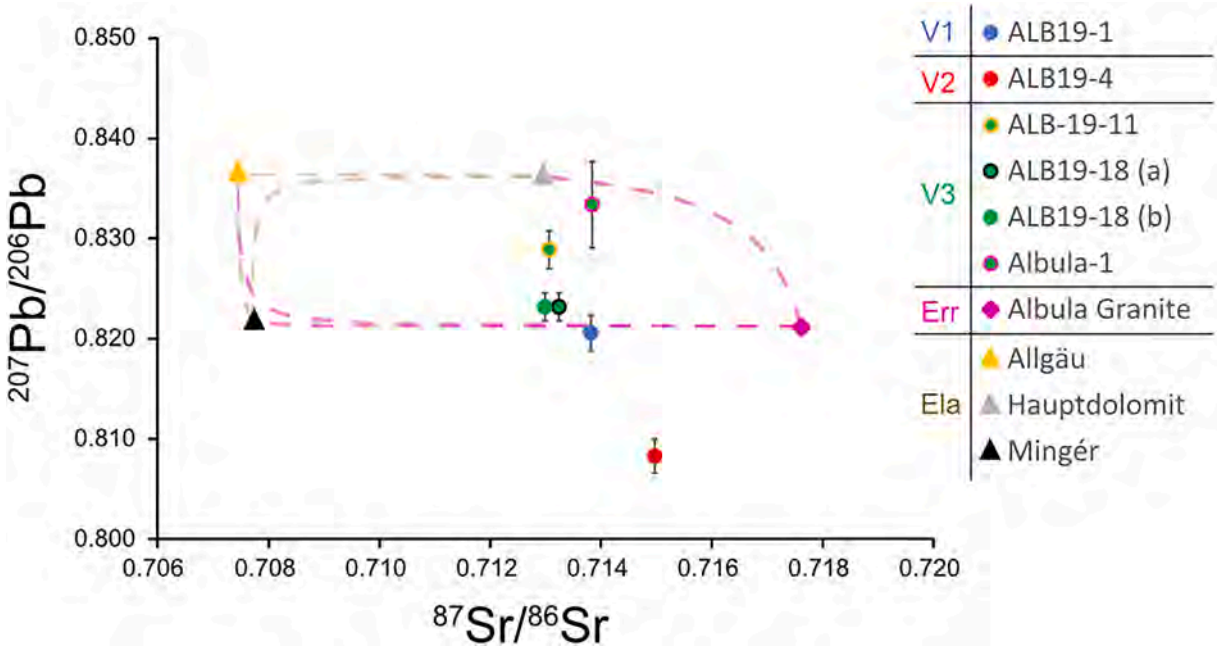

Fig. 10. $^{207}Pb/^{206}Pb$ and $^{87}Sr/^{86}Sr$ data of epidote, Albula Granite and carbonate rocks of the Ela nappe at the time of veining (85–60 Ma). $^{207}Pb/^{206}Pb$ ratios of epidote are by LA-ICP-MS. $^{87}Sr/^{86}Sr$ ratios of epidote and Albula Granite are by TIMS. $^{87}Sr/^{86}Sr$ ratios of carbonate rocks, and $^{207}Pb/^{206}Pb$ ratios of Albula Granite and carbonate rocks are by Neptune MC-ICP-MS. The dashed curves are mixing curves between single rocks samples, calculated using the isotope ratios of Table 3, and Pb and Sr concentrations of Table B1. Error bars are 2 S.E., and smaller than the symbol if not shown.

Table 4
Calculated δD and $\delta^{18}O$ values of the epidote-forming fluids at the temperature of epidote crystallization ($T_{cryst.}$).

	Epidote	Measured δD	δD at $T_{cryst.}$ [1]	Measured $\delta^{18}O$	$\delta^{18}O$ at $T_{cryst.}$ [1]
V1 fluid	ALB19–1	-59 ‰	−38 to −21 ‰	8.5 ‰	5.1–8.2 ‰
V2 fluid	ALB19–4	−52 ‰	−21 to −11 ‰	12.7 ‰	11.4–12.8 ‰
V3 fluids	ALB19–11	−49 ‰	−28 to −11 ‰	7.4 ‰	4.0–7.1 ‰
	ALB19–18 (a)[2]	−47 ‰	−26 to −9 ‰	9.4 ‰	6.0–9.1 ‰
	Albula-1[3]	−48 ‰	−24 to −10 ‰	7.6 ‰	4.3–7.3 ‰
			All ±3 ‰		All ±0.3 ‰

[1] The stable isotope compositions of V1 and V3 epidote-forming fluids are calculated at $T_{cryst.}$ of 270 ± 50 °C based on the chemical composition of chlorite in V3 vein ALB19–11, while those of V2 epidote-forming fluids at $T_{cryst.}$ of 300–350 °C based on literature data (Handy et al., 1996).
[2] δD and $\delta^{18}O$ data of domain (b) of sample ALB19–18 were not collected because pure epidote grains could not be separated.
[3] "Vein1" of Peverelli et al. (2021).

Chacko et al. (1999), respectively. The temperature of crystallization of V3 epidote is calculated from the chemical composition of chlorite in V3 vein ALB19–11 (Sect. 4.4). The chlorite structural formula (Table C1, Appendix C) indicates an average temperature of 270 (± 50) °C for epidote crystallization during V3 veining ca. 60 Ma. This is consistent with the temperature range at the base of the Err nappe during the Ducan–Ela phase (Table 1; Handy et al., 1996).

The temperature of epidote crystallization in V2 vein ALB19–4 can only be estimated by assuming thermal equilibration of the V2 epidote-forming fluids with the country rock. Hence, the temperature range of 300–350 °C existing at the base of the Err nappe during the Trupchun phase (Handy et al., 1996) is used to calculate the $\delta^{18}O$ and δD of the V2 epidote-forming fluid.

Because we do not have an age for V1 epidote, we use the same crystallization temperature of V3 veins (270 ± 50 °C). The use of this value is justified because (1) only the Trupchun and Ducan–Ela phases occurred in the stability field of epidote, excluding that this vein formed in the following lower-temperature Blaisun phase, (2) the isotope data of V1 epidote ALB19–1 are similar to those of V3 epidote and clearly different than V2 epidote, suggesting that V1 epidote formed during the same veining event of V3 epidote (see Sect. 6.2). The calculated δD and $\delta^{18}O$ data of epidote-forming fluids are plotted in Fig. 11 with meteoric line and fields of common water reservoirs from Sheppard (2018). The δD values of all epidote-forming fluids are within uncertainty of each other, ranging between −38 and − 9 (± 3) ‰. On the other hand, $\delta^{18}O$ data are clearly different between V3 + V1 (4.0–9.1 ± 0.3 ‰) and V2 (11.4–12.8 ± 0.3 ‰) epidote-forming fluids.

6. Discussion

6.1. Eo-Alpine fluid circulation revealed by epidote U—Pb ages

The Err nappe bears Sr and O isotopic evidence for seawater circulation in Jurassic times along *syn*-rift faults into the crust (Fig. 12;

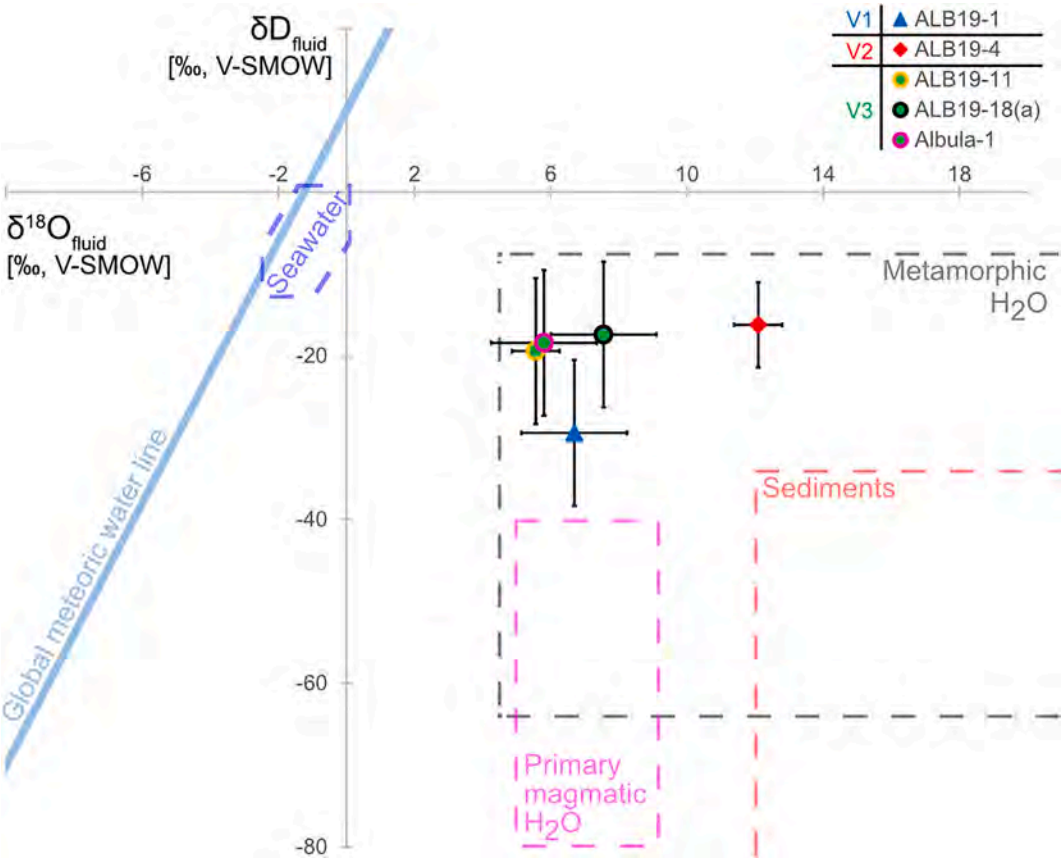

Fig. 11. $\delta^{18}O$ and δD data of epidote-forming fluids calculated from measurements in epidote using, respectively, Zheng (1993) and Chacko et al. (1999). Data of water reservoirs are from Sheppard (2018).

Incerpi et al., 2017, 2018, 2020; Manatschal et al., 2000, 2015; Pinto et al., 2015). In the Albula Pass area, evidence for Jurassic faulting is provided by the presence of syn-rift Saluver breccia (Fig. 2; Froitzheim et al., 1994; Mohn et al., 2011). Therefore, an assumption could be made that all hydrothermal features nearby – epidote veins included – are related to rifting and Jurassic in age. The Late Cretaceous to Paleocene ages (Fig. 12) obtained in this study show that this is not the case. The V2 epidote age of 85.2 ± 9.7 Ma overlaps with the Trupchun phase (88–80 Ma; Handy et al., 1996) of west-directed nappe stacking, while the formation of V3 epidote veins at 59.9 ± 2.7 Ma can be ascribed to the Ducan–Ela extensional phase (80–67 Ma; Handy et al., 1996) in the opposite direction (top-to-the-E; Froitzheim et al., 1994; Handy et al., 1996), which is the youngest deformation phase occurring in the epidote stability field (Table 1; Handy et al., 1996). Although the sampling location is in an area affected by Jurassic rifting, where seawater-driven alteration can produce epidote (e.g., Gardien and Paquette, 2004), all epidote ages are related to the history of Eo-Alpine tectonic inversion of the Adriatic passive continental margin. Particularly, V3 veins were collected next to a Jurassic breccia along which seawater may have circulated, hence the most suitable location where Jurassic epidote veins may have formed. Although it cannot be excluded that Jurassic epidote veins exist and were not sampled, given the small number of studied epidote veins, the dated epidote samples still provide evidence for fluid circulation events that had never been demonstrated before.

Hydration of the granitic crust of the Adriatic passive continental margin occurred at least in three stages (Fig. 12): (1) one related to rifting in the Jurassic (Manatschal et al., 2000, 2015; Pinto et al., 2015; Incerpi et al., 2017, 2018, 2020), and (2–3) two others related to the Eo-Alpine orogeny in Late Cretaceous to Paleocene times as shown here. The combination of data extracted from different hygrochronometers and isotope tracers highlights multi-stage hydrothermal activity in the Adriatic passive continental margin between Jurassic times and at least the Paleocene. It is enticing that so-far undetected events of fluid circulation in an area where hydrothermal activity had already been well characterized is revealed only now by epidote as a newly established geo−/hygrochronometer.

6.2. Discussion of isotope data

As discussed in detail in the following, the Pb–Sr–O–H isotope data of the studied epidote samples are consistent with (1) one fluid pathway with distinct fluid source(s) in the Late Cretaceous, and (2) another fluid pathway and with other fluid sources in the Paleocene. The isotopic similarities between V3 and V1 epidote samples suggest that the undatable V1 epidote vein also formed in Paleocene times, hence defining a V3 + 1 veining event ca. 60 Ma.

6.2.1. Pb–Sr–O–H isotope data and water–rock interaction

The PbSr isotope data of the studied epidote samples are outside the uncertainty of the age-corrected (i.e., 85–60 Ma) $^{207}Pb/^{206}Pb$–$^{87}Sr/^{86}Sr$ ratios of the Albula Granite (Fig. 10). This indicates that the Pb and —Sr isotope systems of epidote-forming fluids were not in equilibrium with the veins' host Albula Granite. Consequently, fluid sources external to the Albula Granite and fluid pathways through other lithologies are required. At the time of V2 and V3 + 1 vein formation, the carbonate rocks of the Ela nappe were both below and above the Err nappe at Albula Pass due to the formation of the Albula steep zone during Trupchun deformation (Froitzheim et al., 1994; Furrer et al., 2015; Handy et al., 1996). In a $^{207}Pb/^{206}Pb$ vs. $^{87}Sr/^{86}Sr$ plot (Fig. 10), the V3 and V1 epidote samples plot in a field defined by isotope mixing curves between carbonate rocks and Albula Granite as endmembers. This allows that the Pb—Sr isotope compositions of the V3 and V1 epidote-forming fluids result from interaction with the Albula Granite after circulation through the carbonate rocks of the Ela nappe. The Sr isotope composition of all epidote samples is dominated by the input from the carbonate rocks of the Ela nappe, given the high Sr mass fractions in these sedimentary rocks relative to the Albula Granite (Table B1). This supports that all (i.e., V1–V3) fluid pathways passed through the carbonate rocks. The $^{87}Sr/^{86}Sr$ isotope composition of V2 epidote-forming fluids plots the closest to that of the Albula Granite at the time of veining, suggesting that these Late Cretaceous fluids interacted with the Albula Granite to a higher extent than the Paleocene ones, possibly due to higher degree of fracturing of cataclastic Albula Granite relative to weakly deformed Albula Granite (Sect. 3).

While the Pb isotope data of V3 and V1 epidote samples plot within the field defined by Albula Granite and carbonate rock endmembers, the $^{207}Pb/^{206}Pb$ ratio of V2 epidote is markedly outside this field. This means that V2 epidote-forming fluids must have interacted with an additional, more radiogenic Pb component. Such a radiogenic Pb component may be acquired from (1) U-rich accessory minerals in Albula Granite or carbonate rocks themselves, or (2) a U-rich lithology other than Albula Granite and carbonate rocks. Because V2 epidote is more radiogenic than V3 + 1 (i.e., lower $^{207}Pb/^{206}Pb$ and higher $^{87}Sr/^{86}Sr$ ratios), it can be excluded that the fluids shared the same fluid pathway at different times, since $^{207}Pb/^{206}Pb$ ratios decrease and $^{87}Sr/^{86}Sr$ ratios naturally increase with time in rocks. Hence, Pb—Sr isotope data indicate that V2 epidote-forming fluids infiltrated the continental crust of the Adriatic passive continental margin via a different fluid pathway than V3 + 1 fluids.

Since oxygen is the most abundant element in rocks, the oxygen isotope composition of the epidote-forming fluids is easily modified by fluid–rock interaction processes and fluid mixing (e.g., Hoef, 2018; Sheppard, 2018). Therefore, the $\delta^{18}O$ values of the epidote-forming fluids do not strictly reflect the O isotope composition of the fluid

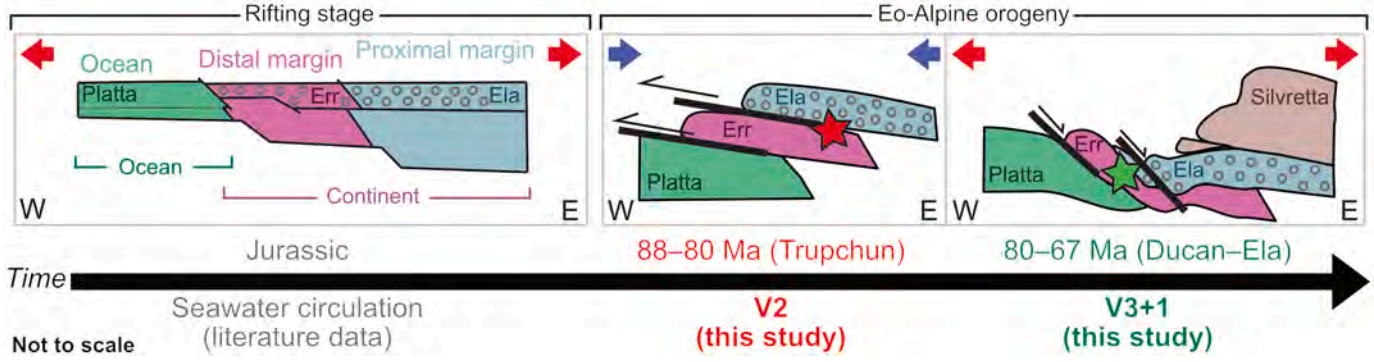

Fig. 12. Sketch of the tectonic regimes affecting the Adriatic passive continental margin and timeline outlining different events of fluid circulation described by previous studies (Incerpi et al., 2017, 2018, 2020; Manatschal et al., 2000, 2015; Pinto et al., 2015) and revealed by this work. Redrawn from Mohn et al. (2011; their Fig. 12). Red and blue arrows indicate, respectively, extension and compression; circles indicate sediments, and filled colors basement of the Ela and Err nappes. Not to scale. (For interpretation of the references to colour in this figure legend, the reader is referred to the web version of this article.)

sources, but rather the modification of fluid $\delta^{18}O$ values during fluid circulation, from the fluid source to the veining location. Conversely, hydrogen is less abundant in granitic and carbonate rocks, as it is mainly stored in hydrous minerals. Fluid δD values are less prone to be modified by fluid–rock interaction, which – in contrast – readily resets the δD values of hydrous phases in rocks (Taylor, 1977, 1978). The lack of evidence for post-veining fluid–epidote interaction (Sect. 3.1) argues against diffusion-driven resetting of the hydrogen isotope system in epidote. Carbonate rocks and granitoids have $\delta^{18}O$ values ranging from 28 to 34 ‰ and 6–10 ‰, respectively (Hoefs, 2004; see also Manatschal et al., 2000). Thus, in a $\delta^{18}O$–δD plot (Fig. 11), the δD values of the epidote-forming fluids can be used "as are" to address fluid sources and mixing of fluids with different sources along fluid pathways, while their $\delta^{18}O$ values must be considered tentatively as they are variably shifted towards higher values during circulation and interaction with carbonate and granitoids.

6.2.2. Plausible fluid sources

Epidote crystallization ages place constraints on the tectonic regime existing during veining, hence unravelling the discussion on possible fluid pathways considering three possible endmembers as fluid sources: (1) metamorphic fluids, (2) modified seawater, and (3) meteoric water. The $\delta^{18}O$–δD values of all epidote-forming fluids overlap with the field of water produced by prograde metamorphic reactions ("metamorphic fluids" in Fig. 11). In the study area, fluids may be released by deeper lithologies, such as serpentinites of the Platta–Lizun–Malenco superunit. Although a small fluid contribution coming from these lithologies cannot be ruled out, the metamorphic conditions reached by the Platta–Lizun–Malenco superunit argue against important dehydration of these rocks (e.g., Handy et al., 1996; Hermann et al., 2000). However, in Jurassic times, the continental crust of the Err nappe was infiltrated by seawater during rifting (Fig. 12; Manatschal et al., 2015; Incerpi et al., 2017, 2018, 2020). Hence, the dissolution of hydrous alteration minerals during Trupchun compression may have produced small amounts of water, which cannot be quantified based on the present data, with a metamorphic signature. The $\delta^{18}O$ composition of the epidote-forming fluids may have originated outside the metamorphic water field and have been shifted towards higher values during fluid circulation, as outlined in Sect. 6.2.1. If this is considered, the original $\delta^{18}O$–δD composition of the epidote-forming fluids may have been consistent with "modified seawater" (i.e., seawater whose O—H isotope composition was shifted towards the right in a $\delta^{18}O$–δD plot by fluid–rock interaction). Given the proximity and the involvement of sedimentary rocks of marine origin in Late Cretaceous deformation (e.g., Froitzheim et al., 1994; Handy et al., 1996), the release of modified seawater during Eo-Alpine deformation is a plausible hypothesis. Finally, the observed stable isotope composition of the epidote-forming fluids may have been produced by meteoric water alone (see Hoefs, 2004; Sheppard, 2018; Campani et al., 2012; Krsnik et al., 2021), which maintained a low δD value but increased its $\delta^{18}O$ value by infiltrating the crust (Sheppard, 2018). Because all epidote-forming fluids are within uncertainty of each other in terms of δD values, but there is a sharp difference between V2 and V3 + 1 $\delta^{18}O$ values, even a fluid source common to V2 and V3 + 1 fluid but exploiting different fluid pathways cannot be ruled out.

7. Eo-Alpine fluid circulation

The structural and paleomorphological situation during the Eo-Alpine orogeny (e.g., elevation, distance from the sea) is not well known. Therefore, we restrict discussion of fluid pathways to identifying the least likely ones in light of the three possible fluid sources identified in Sect. 6.2.2. As confirmed by the Pb—Sr isotope composition of all epidote-forming fluids (Fig. 10), every plausible fluid pathway must traverse the carbonate rocks of the Ela nappe. It must also be kept in mind that, after the formation of the Albula steep zone in the Late Cretaceous, fluid interaction with sedimentary units of the Ela nappe is possible either with a shallower (i.e., downwards fluid circulation) or a deeper (i.e., upwards fluid circulation) origin of the epidote-forming fluids with respect to the Err nappe.

7.1. Trupchun phase veining

V2 veining occurred under a compressional regime during the Trupchun phase (Fig. 12). The base of the Err nappe, at this time, reached ca. 300–350 °C and 800–900 MPa (Table 1; Handy et al., 1996). The initial $^{207}Pb/^{206}Pb$ ratio of Late Cretaceous fluids reveals a radiogenic component inherited by the fluids either at their source or during fluid circulation. Uranium mass fractions of marine carbonate rocks (Table B1) and serpentinized ultramafics (e.g., Deschamps et al., 2013) are typically low, excluding such rocks as potential sources of radiogenic Pb components. Therefore, the most plausible explanation is that the Late Cretaceous fluids were expelled from compacted Jurassic marine sedimentary rocks below the base of the Err nappe during the formation of the Albula steep zone, percolated upwards through carbonate rocks of the Ela nappe into the Err nappe where they acquired a radiogenic Pb isotope compositions. This is supported not only by stable isotope data, but also by the influence of the Ela nappe in the $^{87}Sr/^{86}Sr$ ratio of Late Cretaceous fluids (Fig. 10). The fluids probably acquired their more radiogenic Pb isotope composition by subsequent interaction with U-rich accessory mineral phases (e.g., zircon, allanite) in the Albula Granite itself (Fig. 13, path 1). An important role of the Albula Granite in determining the Pb—Sr isotope composition of Late Cretaceous epidote-forming fluids is supported by the cataclastic texture of the Albula Granite hosting V2 epidote veins (Fig. 6b, red arrow), in that grain-size reduction enhances fluid–rock interaction processes (Putnis, 2021), as well as permeability for fluid circulation in a compressional regime (e.g., Bucher and Stober, 2010; Sibson, 1994, 1996; Yardley and Bodnar, 2014). V2 epidote veins cutting the cataclastic portions of the rock argue that cataclasis of, and white mica crystallization in, the Albula Granite occurred prior to veining. Because white mica is a hydrous mineral, fluids were stored in the Albula Granite before Late Cretaceous veining, and may have been available for recycling via dissolution–precipitation processes during Trupchun deformation. Deformation of hydrothermally altered rocks may promote fluid recycling by the occurrence of dissolution(±precipitation) processes of hydrous minerals (e.g., Peverelli et al., 2022b). Therefore, it is possible that Late Cretaceous epidote-forming fluids contain a recycled component, inherited from the dissolution of hydrous alteration minerals during deformation of the Albula Granite. The present data do not allow to draw firm conclusions in this respect. Development of new robust hygrochronometers (see Bosse and

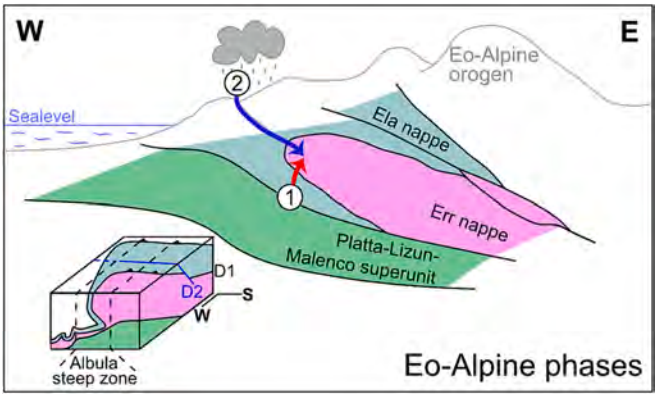

Fig. 13. Sketch of fluid circulation in the study area during the Eo-Alpine orogeny. The white and blue arrows indicate possible fluid sources (1–2), as described in the text. The cross section is redrawn from Mohn et al. (2011; their Fig. 12a); the block diagram is redrawn from Froitzheim et al. (1994; their Fig. 16). Not to scale. (For interpretation of the references to colour in this figure legend, the reader is referred to the web version of this article.)

Villa, 2019) and isotope tracers which can be applied to feldspar alteration products themselves have the potential to provide methodological breakthroughs on such processes of water recycling.

7.2. Ela-Ducan veining

V3 + 1 veining is ascribed to the extensional Ela–Ducan phase (Fig. 12), in which *P–T* conditions at the base of the Err nappe reached 400–500 MPa and 250–300 °C (Table 1; Handy et al., 1996). At this time, normal faults dissected all stratigraphic levels (Froitzheim et al., 1994; Handy et al., 1996). In this geodynamic context, it is possible that fluid percolated along extensional normal faults and infiltrated the continental crust from the surface. Similar scenarios of downward fluid circulation along faults are common (e.g., Dusséaux et al., 2022; Grambling et al., 2022; Incerpi et al., 2018, 2020; Manatschal et al., 2000). The V3 sampling location is close to a preserved Jurassic normal fault filled with Mesozoic *syn*-rift sediments and Albula Granite clasts (i.e., Salver Breccia; Fig. 2). This suggests the existence of exploitable pathways from the surface through the carbonate rocks of the Ela nappe into the Err nappe. It also permits extensive fluid interaction with carbonate rocks by percolation through not only the stratigraphic sequence of the Ela nappe on top of the Err nappe, but also the Saluver breccia itself. Such a fluid pathway (Fig. 13, path 2) well accounts for the Pb—Sr isotope composition of the Paleocene epidote-forming fluids (Fig. 10). Likely fluid sources are modified seawater and meteoric water, or a mixture of these two endmembers. Given the extensional geodynamic regime during the Paleocene and the existence of crustal-scale normal faults, meteoric water was likely the dominant water type causing Paleocene veining. Although no information is available regarding the position of the water table in the area at this time, syn-kinematic meteoric water infiltration along a detachment zone was described by Dusséaux et al. (2022) and it is therefore a possible scenario in orogens. A formation/connate water component may have been left over in the (marine) Mesozoic sediments despite compaction in the Trupchun phase, or water may have been released by deformation-driven dissolution of hydrous alteration minerals that formed during the rifting stage in the Albula Granite. The present scenario permits the addition of recycled fluids to newly introduced ones in the hydration of the continental crust in orogens. If rock-forming minerals in granitoids react with percolating fluids at different stages (Plümper et al., 2017; Taylor, 1977, 1978), then the average isotope composition of the granitic continental crust is repeatedly modified and eventually re-homogenized by orogenic processes.

8. Epidote hygrochronology and outlook

The application of epidote U—Pb dating by LA-ICP-MS is a recent application (Peverelli et al., 2021). However, it has already proven decisive to unravel fluid circulation in the continental crust (Swiss Alps, Heyuan Fault in China, Colombian Andes; Peverelli et al., 2021, 2022a; Siachoque et al., 2023). This study, in addition to confirming the potential of epidote as a hygrochronometer, endorses this mineral as a powerful isotope tracer to investigate fluid sources and pathways (e.g., Peverelli et al., 2022a). Although all applications of epidote U—Pb geochronology are limited to granitoid-hosted epidote (Buick et al., 1999; Oberli et al., 2004 Peverelli et al., 2021, 2022a; Siachoque et al., 2023), preliminary U—Pb isotope data obtained from epidote in mafic rocks from the Belvidere Mountain Complex (Vermont, USA; Peverelli et al., 2023) argues that this geochronometer can provide temporal constraints in geochemical systems that are notably challenging for U—Pb geochronology due to low U contents. A better understanding of epidote trace element data (e.g., Anenburg et al., 2015; Peverelli et al., 2022b) in relation with fluid sources and pathways may provide us with a potent – and not easily reset (Peverelli et al., 2022a, 2022b) – geochemical and geochronological tool recording fluid-assisted processes that are not documented by any other geochronometer or by minerals with low preservation potential.

9. Conclusions

We applied U—Pb geochronology to complement the history of fluid circulation of an inverted passive continental margin. Although the rifting phase had been described by previous studies, geochronological data regarding syn-orogenic fluids were lacking. As shown here, hydration of the continental crust in the Adriatic passive margin continued after tectonic inversion with at least two hydration events during the Eo-Alpine orogeny. Epidote Pb—Sr isotope data show that, before reaching the veining locations in the Albula Granite, Eo-Alpine fluids interacted with syn-rift carbonate rocks of the Ela nappe. Stable isotope geochemistry of epidote suggests that the Late Cretaceous fluids were mainly produced by compaction of Jurassic marine sediments, and the Paleocene ones by meteoric water. In both cases, the predominant fluid component was mixed with recycled fluids, such as those previously stored in marine sediments and/or hydrous alteration minerals during syn-rift fluid circulation. Epidote isotope geochemistry shows that pre-orogenic conditioning of the continental crust of the Adriatic passive continental margin played a role in determining the composition of syn-orogenic fluids. Finally, our data show that to produce a fluid from different endmember waters, it is not imperative that both endmembers circulate at the same time. On the contrary, fluid circulation during orogenic phases itself may promote the recycling, redistribution and homogenization of multiple and different water types in the continental crust in orogens. Notably, the present work is based on geochronological and isotopic data extracted from one mineral only. The multi-methodological approach used here allows for more thorough insight into fluid circulation in deformed, primarily water-poor crustal rocks such as granitoids. In this respect, using epidote to date and trace hydrothermal events in the crust adds useful information about lower greenschist-facies fluid cycling, common in many orogens. This work demonstrates that epidote is an incredibly powerful hygrochronometer and isotope tracer, which has repeatedly complemented the history of fluid circulation in inverted passive continental margins by exposing previously unknow events of fluid circulation.

Authors contribution

VP collected all samples except for epidote vein Albula-1 and the Hauptdolomit sample, prepared all samples for all analytical techniques, characterized the samples, acquired SEM images, carried out EPMA analyses, performed U—Pb dating of epidote, dissolved the samples for solution MC-ICP-MS and TIMS, measured Pb and Sr isotope data by solution MC-ICP-MS and TIMS, did all data reduction and prepared the manuscript. AB and MH supervised the work, helped to structure the manuscript, provided invaluable insight into the structural and tectonic framework of the study area, and collected sample Albula-1 and the Hauptdolomit hand sample, respectively. MW supervised the work in the clean laboratory, analyses by solution MC-ICP-MS and TIMS, and helped organize and interpret Pb and Sr isotope data. AM arranged H isotope measurements and assisted the interpretation of H isotope data. BP performed O isotope measurements, carried out data reduction and guided data interpretation. PL provided technical assistance during microprobe measurements, calculated crystallization temperatures based on EPMA chemical data and provided CAP^{b} allanite grains. TP assisted data interpretation, helped structure the manuscript and granted access to the LA-ICP-MS lab. All authors read the manuscript and contributed to its improvement.

Declaration of Competing Interest

The authors declare no conflicts of interest.

Acknowledgements

The authors thank Catherine Mottram and Tyler Grambling for their constructive reviews and useful suggestions, and Nadia Malaspina for handling the manuscript. We acknowledge the technical assistance of Francesca Piccoli in the LA-ICP-MS lab and Ulrich Treffert for H isotope measurements. We are thankful to Lorenz K. Gfeller of the Geography Department of University of Bern for measuring Rb, Sr, Pb and U contents. We thank Daniela Rubatto for providing CAP and Tara allanite grains, and Klaus Mezger for his unofficial review of the manuscript. VP thanks Thomas Gusmeo for checking the manuscript for clarity before submission. We acknowledge funding of the new LA-ICP-MS facility through the Swiss National Science Foundation, project 206021_170722, to Daniela Rubatto and Thomas Pettke. The solution ICP-MS isotope data were obtained on a Neptune MC-ICP mass spectrometer acquired with funds from the NCCR PlanetS supported by the Swiss National Science Foundation under grant no. 51NF40-141881. This work is part of the PhD thesis of Veronica Peverelli, which was funded by the Swiss National Science Foundation (project 178785 granted to Alfons Berger).

Appendix A. Supplementary data

Supplementary data to this article can be found online at https://doi.org/10.1016/j.lithos.2023.107391.

References

Airaghi, L., Bellahsen, N., Dubacq, B., Chew, D., Rosenberg, C., Janots, E., Waldner, M., Magnin, V., 2020. Pre-orogenic upper crustal softening by lower greenschist facies metamorphic reactions in granites of the Central Pyrenees. J. Metamorph. Geol. 38, 183–204. https://doi.org/10.1111/jmg.12520.

Anenburg, M., Katzir, Y., Rhede, D., Jöns, N., Bach, W., 2015. Rare earth element evolution and migration in plagiogranites: a record preserved in epidote and allanite of the Troodos ophiolite. Contrib. Mineral. Petrol. 169 (3) https://doi.org/10.1007/s00410-015-1114-y.

Barth, S., Oberli, F., Meier, M., 1994. ThPb versus UPb isotope systematics in allanite from co-genetic rhyolite and granodiorite: implications for geochronology. Earth Planet. Sci. Lett. 124, 149–159. https://doi.org/10.1016/0012-821X(94)00073-5.

Bellahsen, N., Bayet, L., Denele, Y., Waldner, M., Airaghi, L., Rosenberg, C., Dubacq, B., Mouthereau, F., Bernet, M., Pik, R., Lahfid, A., Vacherat, A., 2019. Shortening of the axial zone, pyrenees: Shortening sequence, upper crustal mylonites and crustal strength. Tectonophysics 766, 433–452. https://doi.org/10.1016/j.tecto.2019.06.002.

Bird, D.K., Spieler, A.R., 2004. Epidote in Geothermal Systems. Trace element geochemistry of epidote minerals. Rev. Mineral. Geochem. 56, 235–300. https://doi.org/10.2138/gsrmg.56.1.235.

Bons, P.D., Elburg, M.A., Gomez-Rivas, E., 2012. A review of the formation of tectonic veins and their microstructures. J. Struct. Geol. 43, 33–62. https://doi.org/10.1016/j.jsg.2012.07.005.

Bosse, V., Villa, I.M., 2019. Petrochronology and hygrochronology of tectono-metamorphic events. Gondwana Res. 71, 76–90. https://doi.org/10.1016/j.gr.2018.12.014.

Bucher, K., Stober, I., 2010. Fluids in the upper continental crust. Geofluids 10, 241–253. https://doi.org/10.1111/j.1468-8123.2010.00279.x.

Burn, M., Lanari, P., Pettke, T., Engi, M., 2017. Non-matrix-matched standardisation in LA-ICP-MS analysis: General approach, and application to allanite Th-U-Pb dating. J. Anal. At. Spectrom. 32, 1359–1377. https://doi.org/10.1039/c7ja00095b.

Campani, M., Mulch, A., Kempf, O., Schlunegger, F., Mancktelow, N., 2012. Miocene paleotopography of the Central Alps. Earth Planet. Sci. Lett. 337–338, 174–185. https://doi.org/10.1016/j.epsl.2012.05.017.

Dahl, P.S., 1997. A crystal-chemical basis for Pb retention and fissiontrack annealing systematics in U-bearing mineral, with implications for geochronology. Earth Planet. Sci. Lett. 150, 277–290.

Dempster, T.J., 1986. Isotope systematics in minerals: biotite rejuvenation and exchange during Alpine metamorphism. Earth Planet. Sci. Lett. 78, 355–367. https://doi.org/10.1016/0012-821X(86)90003-8.

Deschamps, F., Godard, M., Guillot, S., Hattori, K., 2013. Geochemistry of subduction zone serpentinites: a review. Lithos 178, 96–127. https://doi.org/10.1016/j.lithos.2013.05.019.

Dusséaux, C., Gébelin, A., Boulvais, P., Ruffet, G., Poujol, M., Cogné, N., Branquet, Y., Mottram, C., Barou, F., Mulch, A., 2022. Timing and duration of meteoric water infiltration in the Quiberon detachment zone (Armorican Massif, Variscan belt, France). J. Struct. Geol. 156 (February) https://doi.org/10.1016/j.jsg.2022.104546.

Elburg, M.A., Bons, P.D., Foden, J., Passchier, C.W., 2002. The origin of fibrous veins: constraints from geochemistry. In: Deformation Mechanisms, Rheology and Tectonics: Current Status and Future Perspectives, 200. Geological Society of London, special publication, pp. 103–118.

Enami, M., Liou, J.G., Mattinson, C.G., 2004. Epidote minerals in high P/T metamorphic terranes: Subduction zone and high- to ultrahigh-pressure metamorphism. Rev. Mineral. Geochem. 56, 347–398. https://doi.org/10.2138/gsrmg.56.1.347.

Faure, G., Assereto, R., Tremba, E.L., 1978. Strontium isotope composition of marine carbonates of Middle Triassic to Early Jurassic age, Lombardic Alps, Italy. Sedimentology 25, 523–543. https://doi.org/10.1111/j.1365-3091.1978.tb02078.x.

Feineman, M.D., Ryerson, F.J., DePaolo, D.J., Plank, T., 2007. Zoisite-aqueous fluid trace element partitioning with implications for subduction zone fluid composition. Chem. Geol. 239, 250–265. https://doi.org/10.1016/j.chemgeo.2007.01.008.

Ferry, J.M., 1979. Reaction mechanisms, physical conditions, and mass transfer during hydrothermal alteration of mica and feldspar in granitic rocks from south-Central Maine, USA. Contrib. Mineral. Petrol. 68, 125–139. https://doi.org/10.1007/BF00371895.

Franz, G., Liebscher, A., 2004. Physical and chemical properties of the epidote minerals - an introduction. Rev. Mineral. Geochem. 56, 1–81. https://doi.org/10.2138/gsrmg.56.1.1.

Frei, D., Liebscher, A., Franz, G., Dulski, P., 2004. Trace element geochemistry of epidote minerals. Rev. Mineral. Geochem. 56, 553–605. https://doi.org/10.2138/gsrmg.56.1.553.

Froitzheim, N., Manatschal, G., 1996. Kinematics of Jurassic rifting, mantle exhumation, and passive-margin formation in the Austroalpine and Penninic nappes (eastern Switzerland). Bull. Geol. Soc. Am. 108, 1120–1133. https://doi.org/10.1130/0016-7606(1996)108<1120:KOJRME>2.3.CO;2.

Froitzheim, N., Schmid, S.M., Conti, P., 1994. Repeated change from crustal shortening to orogen-parallel extension in the Austroalpine units of Graubünden. Eclogae Geol. Helv. 87 (2), 559–612.

Furrer, H., Froitzheim, N., Maisch, M., Heierli, H., 2015. Blatt 1237 Albulapass, Geol. Atlas Schweiz 1:25 000, Erläut. 81, Federal Office of Topography swisstopo, Bern, Switzerland.

Gardien, V., Paquette, J.L., 2004. Ion microprobe and ID-TIMS U-Pb dating on zircon grains from leg 173 amphibolites: evidence for Permian magmatism on the West Iberian margin. Terra Nova 16, 226–231. https://doi.org/10.1111/j.1365-3121.2004.00554.x.

Goncalves, P., Oliot, E., Marquer, D., Connolly, J.A.D., 2012. Role of chemical processes on shear zone formation: an example from the grimsel metagranodiorite (Aar massif, Central Alps). J. Metamorph. Geol. 30, 703–722. https://doi.org/10.1111/j.1525-1314.2012.00991.x.

Grambling, T.A., Jessup, M.J., Newell, D.L., Methner, K., Mulch, A., Hughes, C.A., Shaw, C.A., 2022. Miocene to modern hydrothermal circulation and high topography during synconvergent extension in the Cordillera Blanca, Peru. Geology 50, 106–110. https://doi.org/10.1130/G49263.1.

Grapes, R.H., Hoskin, P.W.O., 2004. Epidote group minerals in low-medium pressure metamorphic terranes. Rev. Mineral. Geochem. 56, 301–345. https://doi.org/10.2138/gsrmg.56.1.301.

Gregory, C.J., Rubatto, D., Allen, C.M., Williams, I.S., Hermann, J., Ireland, T., 2007. Allanite micro-geochronology: a LA-ICP-MS and SHRIMP U-Th-Pb study. Chem. Geol. 245, 162–182. https://doi.org/10.1016/j.chemgeo.2007.07.029.

Handy, M.R., Herwegh, M., Kamber, B.S., Tietz, R., Villa, I.M., 1996. Geochronologic, petrologic and kinematic constraints on the evolution of the Err-Platta boundary, part of a fossil continent-ocean suture in the Alps (eastern Switzerland). Schweiz. Mineral. Petrogr. Mitt. 76, 453–474.

Hermann, J., Müntener, O., Scambelluri, M., 2000. The importance of serpentinite mylonites for subduction and exhumation of oceanic crust. Tectonophysics 327, 225–238. https://doi.org/10.1016/S0040-1951(00)00171-2.

Hoef, J., 2018. Stable isotope geochemistry, 2018. Springer International Publishing AG, part of Springer Nature. https://doi.org/10.1016/s0037-0738(97)00056-0.

Hofmann, B.A., Helfer, M., Diamond, L.W., Villa, I.M., Frei, R., Eikenberg, J., 2004. Topography-driven hydrothermal breccia mineralization of Pliocene age at Grimsel Pass, Aar massif, Central Swiss Alps. Schweiz. Mineral. Petrogr. Mitt. 84, 271–302.

Horwitz, E., Dietz, M.L., Chiarizia, R., 1992. The application of novel extraction chromatographic materials to the characterization of radioactive waste solutions. J. Radioanal. Nucl. Chem. 161, 575–583.

Incerpi, N., Martire, L., Manatschal, G., Bernasconi, S.M., 2017. Evidence of hydrothermal fluid flow in a hyperextended rifted margin: the case study of the err nappe (SE Switzerland). Swiss J. Geosci. 110, 439–456. https://doi.org/10.1007/s00015-016-0235-2.

Incerpi, N., Martire, L., Bernasconi, S.M., Manatschal, G., Gerdes, A., 2018. Silica-rich septarian concretions in biogenic silica-poor sediments: a marker of hydrothermal activity at fossil hyper-extended rifted margins (err nappe, Switzerland). Sediment. Geol. 378, 19–33. https://doi.org/10.1016/j.sedgeo.2018.10.005.

Incerpi, N., Martire, L., Manatschal, G., Bernasconi, S.M., Gerdes, A., Czuppon, G., Palcsu, L., Karner, G.D., Johnson, C.A., Figueredo, P.H., 2020. Hydrothermal fluid flow associated to the extensional evolution of the Adriatic rifted margin: Insights from the pre- to post-rift sedimentary sequence (SE Switzerland, N ITALY). Basin Res. 32, 91–115. https://doi.org/10.1111/bre.12370.

Kralik, M., Clauer, N., Holnsteiner, R., Huemer, H., Kappel, F., 1992. Recurrent fault activity in the Grimsel Test Site (GTS, Switzerland) : revealed by Rb-Sr, K-Ar and tritium isotope techniques. J. Geol. Soc. 149, 293–301. https://doi.org/10.1144/gsjgs.149.2.0293.

Krsnik, E., Methner, K., Campani, M., Botsyun, S., Mutz, S.G., Ehlers, A., Kempf, O., Fiebig, J., Schlunegger, F., Mulch, A., 2021. Miocene high elevation and high relief in the Central Alps. Solid Earth 12, 2615–2631. https://doi.org/10.5194/se-12-2615-2021.

Lanari, P., 2012. P-T-e Micro-Mapping in Metamorphic Rocks. Application to the Alps and the Himalaya. Ph.D. Thesis. University of Grenoble, p. 544.
Ludwig, K.R., 2012. User's Manual for a Geochronological Toolkit for Microsoft Excel, 5. Berkeley Geochronology Center. Options.
Manatschal, G., Nievergelt, P., 1997. A continent-ocean transition recorded in the err and Platta nappes (Eastern Switzerland). Eclogae Geol. Helv. 90, 3–27.
Manatschal, G., Marquer, D., Früh-Green, G.L., 2000. Channelized fluid flow and mass transfer along a rift-related detachment fault (Eastern Alps, Southeast Switzerland). Bull. Geol. Soc. Am. 112, 21–33. https://doi.org/10.1130/0016-7606(2000)112<21:CFFAMT>2.0.CO;2.
Manatschal, G., Lavier, L., Chenin, P., 2015. The role of inheritance in structuring hyperextended rift systems: some considerations based on observations and numerical modeling. Gondwana Res. 27, 140–164. https://doi.org/10.1016/j.gr.2014.08.006.
Marquer, D., Burkhard, M., 1992. Fluid circulation, progressive deformation and mass-transfer processes in the upper crust: the example of basement-cover relationships in the External Crystalline Massifs, Switzerland. J. Struct. Geol. 14 (8–9), 1047–1057.
Marquer, D., Peucat, J.J., 1994. Rb-Sr systematics of recrystallized shear zones at the greenschist- amphibolite transition: examples from granites in the Swiss Central Alps. Schweiz. Mineral. Petrogr. Mitt. 74, 343–358.
McArthur, J.M., Howarth, R.J., Shields, G.A., 2012. Strontium isotope stratigraphy. Geol. Time Scale 2012, 127–144. https://doi.org/10.1016/B978-0-444-59425-9.00007-X.
Mohn, G., Manatschal, G., Masini, E., Müntener, O., 2011. Rift-related inheritance in orogens: a case study from the Austroalpine nappes in Central Alps (SE-Switzerland and N-Italy). Int. J. Earth Sci. 100, 937–961. https://doi.org/10.1007/s00531-010-0630-2.
Mohn, G., Manatschal, G., Beltrando, M., Masini, E., Kusznir, N., 2012. Necking of continental crust in magma-poor rifted margins: evidence from the fossil Alpine Tethys margins. Tectonics 31, 1–28. https://doi.org/10.1029/2011TC002961.
Morad, S., El-Ghali, M.A.K., Caja, M.A., Sirat, M., Al-Ramadan, K., Manurberg, H., 2010. Hydrothermal alteration of plagioclase in granitic rocks from Proterozoic basement of SE Sweden. Geol. J. 45, 105–116. https://doi.org/10.1002/gj.1178.
Mulch, A., Teyssier, C., Cosca, M.A., Vennemann, T.W., 2006. Thermomechanical analysis of strain localization in a ductile detachment zone. J. Geophys. Res. Solid Earth 111, 1–20. https://doi.org/10.1029/2005JB004032.
Nägler, T.F., Kamber, B.S., 1996. A new silicate dissolution procedure for isotope studies on garnet and other rock forming minerals. Schweiz. Mineral. Petrogr. Mitt. 76, 75–80. https://doi.org/10.5169/seals-57688.
Oberli, F., Meier, M., Berger, A., Rosenberg, C.L., Gieré, R., 2004. U-Th-Pb and 230Th/238U disequilibrium isotope systematics: Precise accessory mineral chronology and melt evolution tracing in the Alpine Bergell intrusion. Geochim. Cosmochim. Acta 68 (11), 2543–2560. https://doi.org/10.1016/j.gca.2003.10.017.
Oliot, E., Goncalves, P., Marquer, D., 2010. Role of plagioclase and reaction softening in a metagranite shear zone at mid-crustal conditions (Gotthard Massif, Swiss Central Alps). J. Metamorph. Geol. 28, 849–871. https://doi.org/10.1111/j.1525-1314.2010.00897.x.
Pettke, T., Diamond, L.W., Kramers, J.D., 2000. Mesothermal gold lodes in the North-Western Alps: a review of genetic constraints from radiogenic isotopes. Eur. J. Mineral. 12, 213–230. https://doi.org/10.1127/ejm/12/1/0213.
Peverelli, V., Ewing, T., Rubatto, D., Wille, M., Berger, A., Villa, I.M., Lanari, P., Pettke, T., Herwegh, M., 2021. U−Pb geochronology of epidote by laser ablation inductively coupled plasma mass spectrometry (LA-ICP-MS) as a tool for dating hydrothermal-vein formation. Geochronology 3, 123–147. https://doi.org/10.5194/gchron-3-123-2021.
Peverelli, V., Berger, A., Mulch, A., Pettke, T., Piccoli, F., Herwegh, M., 2022a. Epidote U–Pb geochronology and H isotope geochemistry trace pre-orogenic hydration of mid-crustal granitoids. Geology. https://doi.org/10.1130/G50028.1.
Peverelli, V., Berger, A., Wille, M., Pettke, T., Lanari, P., Villa, I.M., Herwegh, M., 2022b. Epidote dissolution – precipitation during viscous granular flow : a micro-chemical and isotope study. Solid Earth 13, 1803–1821. https://doi.org/10.5194/se-13-1803-2022.
Peverelli, V., Vitale Brovarone, A., Olivieri, O.S., Piccoli, F., 2023. Dating the migration of high-pressure H_2-/CH_4-bearing fluids in subduction zones. In: Goldschmidt Conference 2023, Lyon (France).
Pinto, V.H.G., 2014. Linking Tectonic Evolution with Fluid History in Hyperextended Rifted Margins: Examples from the Fossil Alpine and Pyrenean Rift Systems, and the Present-Day Iberia Rifted Margin. Ph.D. Thesis. University of Strasbourg, p. 256.
Pinto, V.H.G., Manatschal, G., Karpoff, A.M., Viana, A., 2015. The example of Alpine Tethyan rifted margins. Geochem. Geophys. Geosyst. 16, 3271–3308. https://doi.org/10.1002/2015GC005830.
Plümper, O., Botan, A., Los, C., Liu, Y., Malthe-Sørenssen, A., Jamtveit, B., 2017. Fluid-driven metamorphism of the continental crust governed by nanoscale fluid flow. Nat. Geosci. 10, 685–690. https://doi.org/10.1038/ngeo3009.
Poli, S., Schmidt, M.W., 2004. Experimental subsolidus studies on epidote minerals. Rev. Mineral. Geochem. 56, 171–195. https://doi.org/10.2138/gsrmg.56.1.171.
Putnis, A., 2021. Fluid-mineral interactions: controlling coupled mechanisms of reaction, mass transfer and deformation. J. Petrol. 62, 1–27. https://doi.org/10.1093/petrology/egab092.
Ricchi, E., Bergemann, C.A., Gnos, E., Berger, A., Rubatto, D., Whitehouse, M.J., 2019a. Constraining deformation phases in the Aar Massif and the Gotthard Nappe (Switzerland) using Th-Pb crystallization ages of fissure monazite-(Ce). Lithos 342–343, 223–238. https://doi.org/10.1016/j.lithos.2019.04.014.
Ricchi, E., Bergemann, C., Gnos, E., Berger, A., Rubatto, D., Whitehouse, M., Walter, F., 2019b. Cenozoic deformation in the Tauern Window (Eastern Alps, Austria) constrained by in-situ Th-Pb dating of fissure monazite. Solid Earth Discuss 1–59. https://doi.org/10.5194/se-2019-162.
Sheppard, S.M.F., 2018. Characterization and isotopic variations in natural waters. Stable Isot. High Temp. Geol. Process. 165–183.
Siachoque, A., Cardona, A., Rodríguez-Cuevas, M., Valencia-Gómez, J.C., Zapata, S., Peverelli, V., Wemmer, K., Valencia, V., 2023. Temporalidad del hidrotermalismo y la deformación durante las fases de "syn-rift" en el Valle Superior del Magdalena usando U–Pb en epidote y titanita y K–Ar en illita. In: XIX Congreso Colombiano de Geologia 2023, Santa Marta (Colombia).
Sibson, R.H., 1994. Crustal stress, faulting and fluid flow. Geol. Soc. Spec. Publ. 78, 69–84. https://doi.org/10.1144/GSL.SP.1994.078.01.07.
Sibson, R.H., 1996. Structural permeability of fluid-driven fault-fracture meshes. J. Struct. Geol. 18 (8), 1031–1042. https://doi.org/10.1016/0191-8141(96)00032-6.
Smye, A.J., Roberts, N.M.W., Condon, D.J., Horstwood, M.S.A., Parrish, R.R., 2014. Characterising the U-Th-Pb systematics of allanite by ID and LA-ICPMS: Implications for geochronology. Geochim. Cosmochim. Acta 135, 1–28. https://doi.org/10.1016/j.gca.2014.03.021.
Taylor, H.P., 1977. Water/rock interactions and the origin of H2O in granitic batholiths. J. Geol. Soc. Lond. 133, 509–558. https://doi.org/10.1144/gsjgs.133.6.0509.
Taylor, H.P., 1978. Oxygen and hydrogen isotope studies of plutonic granitic rocks. Dev. Petrol. 5, 177–210. https://doi.org/10.1016/B978-0-444-41658-2.50014-6.
Vidal, O., Parra, T., Vieillard, P., 2005. Thermodynamic properties of the Tschermak solid solution in Fe-chlorite: Application to natural examples and possible role of oxidation. Am. Mineral. 90, 347–358. https://doi.org/10.2138/am.2005.1554.
Vidal, O., De Andrade, V., Lewin, E., Munoz, M., Parra, T., Pascarelli, S., 2006. P-T-deformation-Fe3+/Fe2+ mapping at the thin section scale and comparison with XANES mapping: Application to a garnet-bearing metapelite from the Sambagawa metamorphic belt (Japan). J. Metamorph. Geol. 24, 669–683. https://doi.org/10.1111/j.1525-1314.2006.00661.x.
Wehrens, P., Berger, A., Peters, M., Spillmann, T., Herwegh, M., 2016. Deformation at the frictional-viscous transition: evidence for cycles of fluid-assisted embrittlement and ductile deformation in the granitoid crust. Tectonophysics 693, 66–84. https://doi.org/10.1016/j.tecto.2016.10.022.
Wehrens, P., Baumberger, R., Berger, A., Herwegh, M., 2017. How is strain localized in a meta-granitoid, mid-crustal basement section? Spatial distribution of deformation in the central Aar massif (Switzerland). J. Struct. Geol. 94, 47–67. https://doi.org/10.1016/j.jsg.2016.11.004.
Weis, D., Kieffer, B., Maerschalk, C., Barling, J., De Jong, J., Williams, G.A., Hanano, D., Pretorius, W., Mattielli, N., Scoates, J.S., Goolaerts, A., Friedman, R.M., Mahoney, J. B., 2006. High-precision isotopic characterization of USGS reference materials by TIMS and MC-ICP-MS. Geochem. Geophys. Geosyst. 7 https://doi.org/10.1029/2006GC001283.
Yardley, B.W.D., Bodnar, R.J., 2014. Fluids in the continental crust. Geochem. Perspect. 3, 1–127. https://doi.org/10.7185/geochempersp.3.1.
Zheng, Y.-F., 1993. Calculation of oxygen isotope fractionation in hydroxyl-bearing silicates. Earth Planet. Sci. Lett. 120, 247–263. https://doi.org/10.1016/0012-821X(93)90243-3.